3-D VELOCITY STRUCTURE OF EASTERN MARMARA REGION FROM LOCAL EARTHQUAKE TOMOGRAPHY

by

Alper Denli

B.S. Geophysical Engineering, İstanbul University, 2004

Submitted to

Boğaziçi University

Kandilli Observatory and Earthquake Research Institute

in partial fulfillment of the requirements for the degree of

Master of Science

Graduate Program in Geophysical Engineering

Boğaziçi University

2008

3-D VELOCITY STRUCTURE OF EASTERN MARMARA REGION FROM LOCAL EARTHQUAKE TOMOGRAPHY

APPROVED BY:

Prof. Dr. Cemil Gürbüz (Thesis Supervisor)	. . . . .
Prof. Dr. Niyazi Türkelli	. . . . .
Prof. Dr. Ali Pınar	. . . . .

DATE OF APPROVAL: ……. June 2008

ACKNOWLEDGEMENT

I would like to express my sincere gratitude to my advisor Prof. Dr. Cemil Gürbüz who have been encouraging me, supporting me, helping me, giving freedom to select and execute my research subject. His invaluable guidance and proffesional excellence throughout my goal provide a motivation to expose this study. I would like to mention his affirmative perspective, giving me inspiration, when I was in a fix.

I am a grateful to Prof. Dr. Edi Kissling for his helpful guidance and significant determinations about my study. His propositions about my performance elicit to complete my study with a self-confidence. I would like to thanks Prof. Dr. Balamir Üçer for his suggestion about data analysis. I would like to express my special thanks to Esen Arpat. Sharing his knowledge about geology and tectonics in the study area contribute to my thesis in a big way. I would like to thank to Mustafa Uğur Teoman who have been with me on this thesis at any moment. I would like to thank to the members of Department of seismology, Boğaziçi University for data collection. I also acknowledge to the members of TÜBITAK-Marmara Research Center, Earth and Marine Sciences Research Institute for providing the data. This work performed with contributions of Boğaziçi University, Research Foundation (Project No:07T204).

I would like to thanks Tuğçe Afacan Ergün and Doğan Aksarı for sustaining me when I needed. I count myself fortunate to have such a genuine friends who help me and take care of me all along. Their intimate friendships and valuable scientific point of views are worthy of many thanks.

I thank all the faculty members and staff of the Boğaziçi University, Department of Geophysics.

I would like to acknowledge the spiritual and material support of my parents who helped me to conceive the importance of education and encouraged me through all my life. This goal would not be realized without their concerns and patiences.

ABSTRACT

3-D VELOCITY STRUCTURE OF EASTERN MARMARA REGION FROM LOCAL EARTHQUAKE TOMOGRAPHY

Local earthquakes located in 40-41.5 N and 28-30.5 E geographic coordinates between the dates January,2003-October,2007 were selected to use for local earthquake tomography. Data were obtained from short period and broadband seismic stations dispersely located in the region.

This study was conducted to reveal 3-D P wave velocity structure in the target area. To prepare data set, relocation procedure was done. To determine the 1-D velocity model for the study region, earthquakes which have azimuthal gap less than 180^0 and recorded at least by 7 stations were selected. Obtained 1-D velocity model has 32 km depth. Reliable solutions were observed to 17 km due to the depth distributions of the earthquakes. To consolidate the robustness of the velocity model, shifting test was applied and quarry blast data were used. Results show that the 1-D velocity model represents the study region. Using reference earth model for local earthquake tomography was decided. Later on, observing more confidential parts of the velocity changes in the study region, synthetic models were produced for the checkerboard test. At the same time, control parameters were set to obtain reasonable solution after running tomography algorithm. 3-D tomographic inversion based on damped least square inversion was applied to 14329 P wave arrival times and the results of 3-D tomographic inversion were tried to correlate with geologic verifications in the region. Generally low velocities change between 5.3-5.7 km/s through vertical extension of the faults. Vertical extensions of the NAF branches are observed between 2 -15 km depths when the resolution parameter of the data set taken into account. These properties are relatively similar for extracted profiles. Location of the vertical extensions of the fault zones mainly show the same depth range similar to done previous studies in the region.

ÖZET

DOĞU MARMARA BÖLGESİNİN 3 BOYUTLU HIZ YAPISININ YEREL DEPREM TOMOGRAFİSİ YÖNTEMİ İLE BELİRLENMESİ

Ocak 2003-Ekim 2007 tarihleri arasında 40-41.5 Kuzey ve 28-30.5 Doğu coğrafi koordinatları arasında kalan saha içerisinde meydana gelmiş olan lokal depremler kullanılarak lokal deprem tomografisi için data seti oluşturulmuştur. Veri dağınık olarak bölge içerisinde konumlandırılmış kısa bant ve geniş bant aralıklı sismik istasyonlar aracılığıyla toplanmıştır.

Bu çalışma bölgenin üç boyutlu P dalgası hız yapısının belirlenmesi amacına yönelik gerçekleştirilmiştir. Bunun için ilk aşamada yer bulma işlemi tamamlanmış, bölgenin bir boyutlu hız yapısını belirlemek amacıyla toplanan depremler kullanılarak bölgenin bir boyutlu hız modeli tayin edilmeye çalışılmıştır. Elde edilen model bölgenin kabuk yapısına uygun olarak 32 km derinliğinde olup depremlerin derinlik dağılımından ötürü 17 km ye kadar güvenilir çözümler gözlenmiştir. Elde edilen bir boyutlu P dalgası hız modelinin güvenilirliğine ilişkin yapılan testler sonucunda modelin bölgenin yapısını temsil ettiğine karar verilmiştir. Daha sonra sentetik modeller üretilerek yapıda hangi alanların nasıl bir çözünürlülükle elde edilebileceği araştırılmıştır. Sentetik modelleme esnasında, algoritmanın kabul edilebilir bir çözüm üretebilmesi için gerekli kontrol parametreleri ayarlanmıştır. Son olarak 14329 P dalgası geliş zamanına sönümlü en küçük kareler yöntemi esasına dayanan üç boyutlu tomografik ters çözüm yöntemi uygulanmıştır. Elde edilen tomografik figürler bölgenin jeolojik yapısı ile ilişkilendirilmeye çalışılmıştır. Genellikle, düşük hız değerleri 5.3-5.7 km/s arasında değişiklik göstermektedir. Kuzey Anadolu Fayının dikey uzantıları yaklaşık olarak 2-15 km derinlik değerleri arasında gözlenmektedir. Bu değer ve yorumlar data setinin çözünürlük parametresi esas alınarak yapılmıştır. Fay zonlarına karşılık geldiği düşünülen düşük hızların konumları bölgede daha önce yapılmış olan çalışmalarla benzerlik göstermektedir.

TABLE OF CONTENT

LIST OF FIGURES

LIST OF TABLES

LIST OF SYMBOLS / ABBREVIATIONS

Z	Jacobian matrix
e	Error vector
g	Discrepancy vector
S	Cumulative squarred error
δ	The parameter change vector
β	Damping parameter
I	Identity matrix
u	slowness
r	residual vector
H	the matrix of hypocenter parameter
Δh	the vector of hypocenter parameter
M	the matrix of velocity parameter
Δm	the vector of velocity parameter
R	Resolution matrix
p	Slowness vector

NAFZ	North Anatolian Fault Zone
NAF	North Anatolian Fault
KOERI	Kandilli Observatory and Earthquake Research Center
TUBITAK	The Scientific & Technological Research Council of Turkey
Mw	Moment Magnitude
GPS	Global Positioning System
N	North
S	South
E	East
W	West

Hz	Hertz
W	Watt
1-D	One Dimensional
2-D	Two Dimensional
3-D	Three Dimensional
ACH	Aki-Christoffersion-Huseybe Method
MTA	Mineral Research and Exploration General Directorate
NORSAR	Norwegian Research Council
USGS	U.S. Geological Survey
ART	Algebraic Reconstruction Technique
SIRT	Simultaneous Iterative Reconstruction Technique
RMS	Root Mean Square
LET	Local Earthquake Tomography
DWS	Derivative Weighted Sum
RDE	Resolution Diagonal Element
RKP	Runga-Kutta Perturbation

1. INTRODUCTION

Seismic tomography produces a map of an object's internal properties in a non-invasive fashion (Radon, 1917). By measuring the travel times of a seismic wave between source and receiver points around a rock mass, it is possible to calculate a map of the distribution of physical properties influencing seismic wave velocity within a rock mass. The word tomography means "slice picture" and was first adapted to the field of medicine (Hounsfield, 1973; Cormack, 1973) and subsequently to the geosciences (Dines and Lytle, 1979). For at least 20 years, tomography has been used in the mining industry to create images of geologic features as well as stress-related features (Buchanan *et al*., 1981, Mason 1981, Kormendi *et al*., 1986). A more recent mining-specific application of tomography is an adaptation which can image stress concentrations ahead of the longwall face by using the longwall shearer itself as the seismic source (Westman *et al*., 1996). In seismology, the first tomography application was applied on earth modelling to determine earth's upper mantle velocity structure via teleseismic events by Aki, Christofferson and Huseybe (1976). Result of the first 3-D tomographic inversion shows that significant velocity changes in medium and important implication on tectonics.

Tomography methods are generally classified into two groups according to data type and distance between source and receiver. There are two types of tomography, uncontrolled and controlled source, which depend on the source type. In uncontrolled source tomography, earthquake data are generally used and deep earth structure can be imaged. Furthermore, focal and velocity parameters should be inverted simultaneously due to indeterminate exact location of the uncontrolled source. Controlled source tomography is generally used for engineering applications. Explosive materials are used as source and shallow structure of the earth can be imaged in controlled source tomography. Tomography methods according to the distance between source and receiver are categorized as local earthquake tomography and teleseismic tomography. Earthquakes and seismic stations are participated in the same model space and seismic velocity of the upper crust is searched in regional scale in local earthquake tomography. In teleseismic tomography, long period seismic waves are used and earth's interior are imaged in global scale. Traveltime and waveform tomography are classified according to data type. In travel time tomography,

seismic slowness along the ray path between source and receiver is calculated through traveltimes in recorded waves and velocity structure is determined by applying some inversion techniques. An inversion method is applied to waveform of seismic trace in waveform tomography and it allows to obtained more detailed information about the earth's interior compared to traveltime tomography by reason of sensibility of amplitudes in seismic signal to velocity changes in medium.

Seismic tomography signifies a revolution in earth sciences. It has deep impacts on the geological community and it will continue to influence the future developments in earth sciences. During the 20th century, seismologists had made a number of important discoveries and still is. The first 3-D inversion method, namely ACH, was developed at an array center called NORSAR in southern Norway by Aki, Christofferson and Husebye in 1974. The extension of the method to the data from local earthquakes was carried out by Aki and Lee (1976) at the regional array center of the USGS at the Menlo Park and the results of these studies showed importance of the method and significant implications on tectonics. The first local earthquake tomography application was performed by Aki *et al*., (1976) with using teleseismic P wave data obtained from seismic array of USGS in middle California in 1974. Aki and Lee (1976) developed to local earthquake tomography to apply it to local earthquakes in 1976. Hirahara (1997) applied the same technique for the upper mantle under Japan for mapping the subducting high velocity Pacific plate. In the coming years iterative matrix solvers were exposed by Clayton and Comer (1983) and Nolet (1985) and it permits a quantum jump in the number of model parameters. The discovery of global seismic image (Dziewonski and Anderson, 1984; Tanimoto and Anderson, 1984; Woodhouse and Dziewonski, 1984) which correlated well with the pattern of geoid, and a successful explanation of the correlation using geodynamics (Hager *et al*., 1985) also very considerable in terms of believability of the seismic tomography. Tomographic images obtained from former studies as per date related to global seismic velocity distirbution which originates from mantle dynamics and jeoid, the structure of subducted plates association with the tectonic evalution, magma volume and geometry in volcanic and geothermal regions and velocity structure in fault zones.

Marmara region is a one of the most tectonically active region on the continents. The intense activity of the NAF and the apparent migration of the earthquake sources along the

fault make the region place of interest for earth scientists. Different sections of NAF show various seismic properties and the fault ruptures of the largest earthquakes propagated into the sections of the fault that have had few moderate earthquakes (Dewey, 1976). These similarities are reminiscent of the San Andreas fault. The 1500 km long NAF which has many characteristics similar to the San Andreas fault is one of the most extensively studied right-lateral strike slip faults in the world (Ketin and Roesli, 1953; Pavoni, 1961; Allen, 1968, 1969; Wallace, 1968). Complex structure of the NAF indicates geologic and tectonic importance of the region and explains that why many geophyscial applications are performed in the region.

In this study, we bordered the targeted area in between 40-41.5 N and 28-30.5 E geographical coordinates. In this area NAF is spread at two branches between Dokurcun and Karapürçek. One branch is passing through İzmit region, Gölcük and Karamürsel. Second branch is passing through the south edge of the İznik Lake to Gemlik. The main purpose of this study is to reveal horizontal velocity changes at different depths and extract vertical depth sections which are crossing the branches of NAF. Observing unknown feasible and former inactive faults in the study region is the other aim of this study. To realize of this aim, length of the vertical cross sections is determined through comparing ray coverage in the study region. Before presenting conclusions of the study, following steps were conducted. Earthquake data set were prepared, all stages of data acquisition and 3-D tomographic inversion process were presented. Later on tomographic images were interpreted.

2. GEOLOGY-TECTONIC SETTINGS AND PREVIOUS STUDIES IN THE REGION

2.1. Geology in the Region

Marmara region is primarily composed of three parts, Sakarya zone, İstanbul zone and Istranca masif (Ketin, 1973 and Okay, 1986). Geologic features in the study area are mainly originates from two parts, Istanbul zone and Sakarya zone.

The İstanbul zone is described by a well developed, unmetamorphosed and little deformed continuous Palezoic sedimantary succession extending from Ordovician to the Carboniferous overlain with a major unconformity by latest Permian to the lowermost Triassic continental red beds. The İstanbul zone is different from the neighbouring tectonic units in its stratigraphy, absence of metamorphism and lack of major deformation. The intra-pontid suture of late Triassic-Early Jurassic age subsists which roughly follows the northern strand of the NAF between İstanbul zone and Sakarya zone (Ketin, 1973 and Okay, 1986).

The Sakarya zone does not have a Paleozoic basement in contrast to the İstanbul zone. The Sakarya zone is characterized by a various metamorphosed and strongly deformed Triassic basement, namely Karakaya Complex overlain with a major unconformity by Liassic conglomerates and sandstones which passes up to Middle Jurassic-Lower Cretaceous limestones and Upper Cretaceous flysch (Hoşgören, 1997). Karakaya Complex of Triassic age made up of strongly deformed metamorphosed basic volcanic rocks, limestones and greywackes with limestone olistoliths forms the basement to the undeformed post-Triassic sediments of the Sakarya zone. The Izmir-Ankara-Erzincan suture separated the Sakarya zone from the Anatolide-Tauride units (Ketin, 1973 and Okay, 1986).

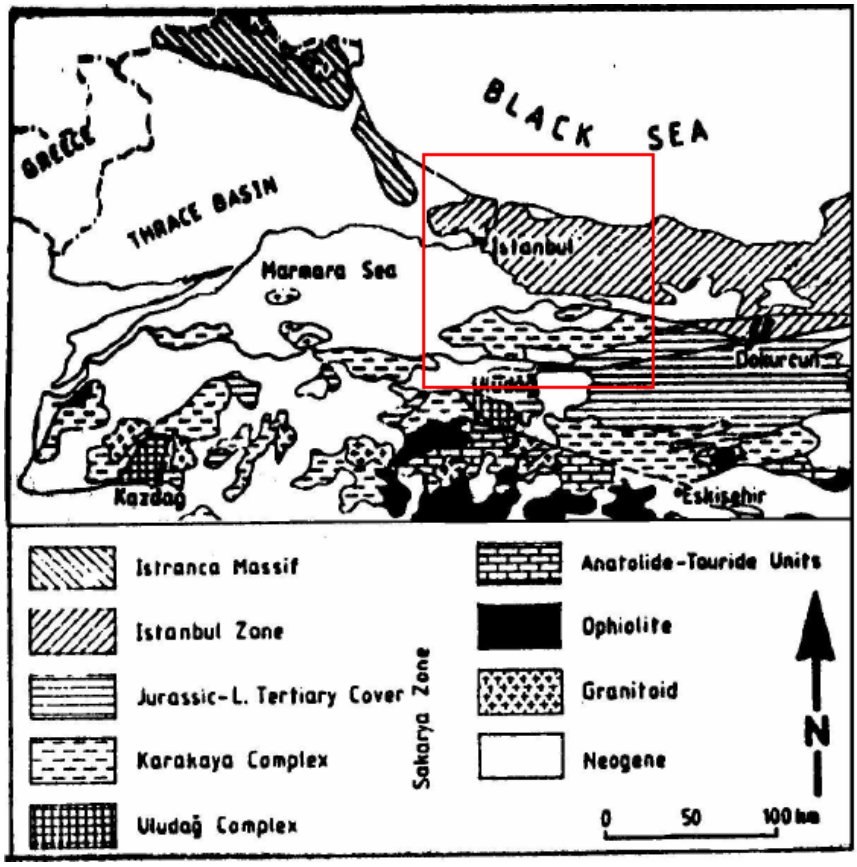

Figure 2.1. Geological units of the Marmara region modified from Ketin (1967) and Okay (1986). Red box shows geologic units in the study region

The internal structure of the Karakaya Complex is not well known (Figure 2.1). However, it is apparently made up of several tectonic units including a thick volcanic section with abundant basic pyroclastics and tuffs intercalated with carbonates, and a greywackes section with Permian and Carboniferous limestone olistoliths. The metamorphism where it occurs is usually in high-pressure greenchist facise, and sodic amphibole occurs frequently in basic volcanic rocks. The deformation is locally semi-brittle giving a broken formation character to the Karakaya Complex. The Karakaya Complex is also intruded by several pre-Liassic granitoids (Hoşgören, 1997).

The İzmit gulf is an east-west trending active graben which is dynamically affected by the interaction of the North Anatolian Fault Zone and the Marmara graben systems. It is bounded by two horsts: the Kocaeli Peninsula to the North and the Armutlu Peninsula to the south, showing completely different geomorphological features, and by well defined

fault scarps. The graben varying between 6 km and 10 km in width is comparatively large, long and narrow basin filled with young seidments of marine and continental facies (Seymen, 1995).

The Kocaeli and Armutlu peninsula stratigraphically, structurally and geologically gave completely different geological features; so that the intra-Pontid suture İstanbul and Sakarya zones defined within the western Pontides is passed along the axis of the graben. Along the Izmit gulf, there are Late Pleistocene (tyrrhenian) age marine terraces and sediment depositions as in Yalova-Lale Dere, Hersek and Karamürsel. In addition to the quaternary deposits along the shores of Izmit Gulf, the vicinity of Sakarya river is covered by alluvial deposits which are generally consisted of loose sand and silt (Hoşgören, 1995).

2.2. Tectonics in the Region

In Turkey, the Anatolian plate is located in the highly active Alpine-Himalayan seismic belt and characterized by the collision of the African and the Arabian plates with the Eurasian plate (McKenzie, 1972), as shown in Figure 2.2. The collision probably started during Early Miocene (Yılmaz *et al*., 1995) and caused to thickening, shortening and uplift of the Anatolian block. The Anatolian Block started to move west over the NAFZ, during Late Miocene to Pliocene before approximately 5.7 million years. The NAFZ is in fact regarded as large-scale transform fault like the San Andreas Fault (Barka, 1992), and has been sited numerous disastrous earthquakes including the Erzincan earthquake of 1939 (Mw7.9), the Izmit (Mw7.4) and the Düzce (Mw7.2) earthquakes of 1999. It is a nearly 1500 km long dextral strike-slip fault extending from Karliova triple junction in the Eastern Turkey, crossing through the Marmara Sea and entering the North Aegean Sea and mainland Greece in the west.

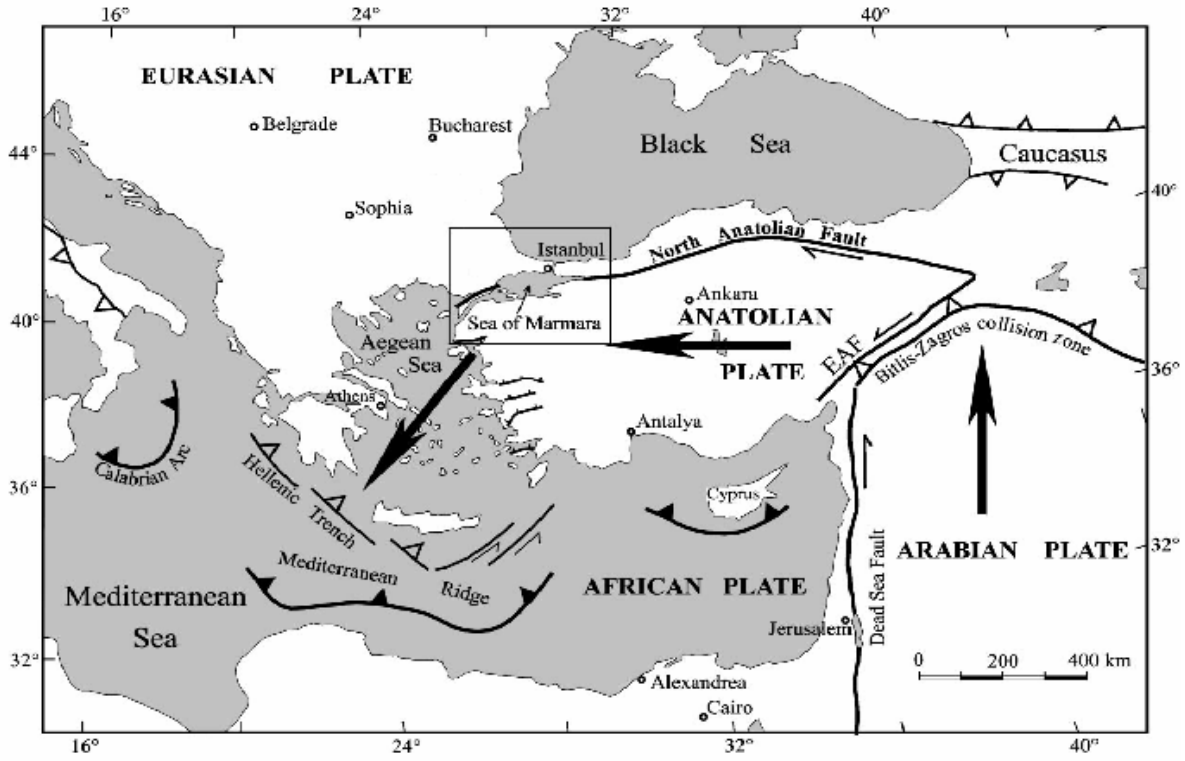

Figure 2.2. Tectonic map of Turkey (Okay *et al*., 2000)

In the eastern part of the Marmara Sea region which composes main part of the study area, the westward motion of Turkey relative to Europe occurs mostly along the North Anatolian Fault zone. East of about longitude 30^0 E, the North Anatolian Fault system, which accommodates most of the westward motion of Turkey, has a narrow and localized character, clearly defined by the predominantly strike-slip surface along its entire 1000-km length, which is associated with a series of major earthquakes (Ambraseys, 2002).

In fact, Marmara region has shown complex tectonic features with high seismic activity (Barka and Kadinsky-Cade, 1988). In particular, the NAFZ zone splays into two main branches around Bolu and then into three branches around Geyve-Adapazarı. The three branches have been called the northern (Sapanca Lake, the Gulf of Izmit, the northern Marmara Sea, Murefte, the Gulf of Saros), the middle (Geyve, the south of Iznik Lake, the west of Gemlik Bay, Bandırma, Ezine) and the southern (Geyve, Edremit) branches (Dewey and Şengör, 1979; Şengör *et al*., 1985).

The Marmara Sea Basin is about 230 km long and 70 km wide with a shallow shelf to the south and a series of subbasins to the north, namely, the Tekirdag, Cinarcik, Karamursel, and Izmit basins. Active faulting on land in the region is relatively well documented. However, the pattern of active faulting in the Basin is much less well established. Originally the Basin was considered to be a graben or a structure of right-lateral faults exhibiting an overall normal motion (Barka and Kadinsky-Cade, 1988). Recently it was proposed that the Marmara Sea Basin was controlled by a strike-slip fault that extended between the Gulf of Izmit and the Galipoli Peninsula (Le Pichon *et al*., 2000). However, its bathymetry, supplemented by faults identified by conventional seismic reflection surveys and focal mechanisms of a few earthquakes (Ambraseys and Jackson, 2000), shows a series of pull-apart basins bounded by a system of relatively short strike-slip and normal faults, which clearly imply significant regional extension responsible for the formation of the Marmara Sea Basin (Smith *et al*., 1995; Wong *et al*., 1995; Parke *et al*., 2000; Okay *et al*., 2000). The rate of tectonic deformation, which is derived from regional space geodetic (Straub and Kahle, 1995; McClusky *et al*., 2000) and seismotectonic slip rate (Canıtez and Üçer, 1967; Eyidoğan, 1988; Taymaz *et al*., 1991) measurements, varies from 1.7 to 2.4 cm/yr right lateral E-W slip across the Marmara region, where the NAFZ splays into a number of branches in and around the İzmit Bay (Dewey and Şengör, 1979; Crampin and Evans, 1986; Wong *et al*., 1995). The NAFZ appears to be more multistranded and discontinuous offshore, within the Sea of Marmara, than onshore (Smith *et al*., 1995; Okay *et al*., 1999).

2.3. Seismicity in the Region

High seismicity is generally observed as clusters at plate boundaries and fault zones in tectonically active regions. To understand the characteristics of NAF seismicity since 1930, Dewey *et al*. (1976) relocated earthquakes associated with the NAF. Many features of the occurence of magnitude 5 and greater earthquakes on the NAF are similar to characteristics of small-earthquake seismicity on California's San Andreas fault. Earthquakes tend to be concentrated on or near particular sections of the NAF, suggesting intrinsic differences in mechanical properties along the fault. The relocated epicenters support the hypothesis that fault rupture in large and great earthquakes will begin in regions of small and moderate earthquakes. The rupture of the large earthquake then

propagates into sections of the fault that normally have a low level activity. Marmara region is an active tectonic zone delineated by the transition between the dextral strike-slip regime of the NAF and the extension regime of the Aegean Sea. To reveal seismotectonic aspect of the Marmara Region, Gürbüz *et al*. (2000) performed the microseismic experiment. The all set of known historical earthquakes is analysed in the context of this study and the observation was made. The most active part of the NAF is the northern branch (Oztin and Bayulke, 1990; Ambraseys and Finkel, 1995) as shown in Figure 2.3 which denote the active faulting in the region, the estimated rupture area of the historical destructive earthquakes of last three centuries, together with the instrumentally recorded large events of this century (Barka, 1997; Üçer *et al*., 1997). The south branch of the fault system, in the interior of the mainland south of the Marmara Basin, is less active than the north branch through İzmit and the Marmara Basin. The morphology of the south branch through Geyve, Bursa, and Gonen to the Aegean Sea suggests late Quaternary activity (Barka, 1996) and a long-term seismicity that accounts for an average shear velocity of about 0.3 cm/yr, which is compatible with GPS measurements (Straub, 1996).

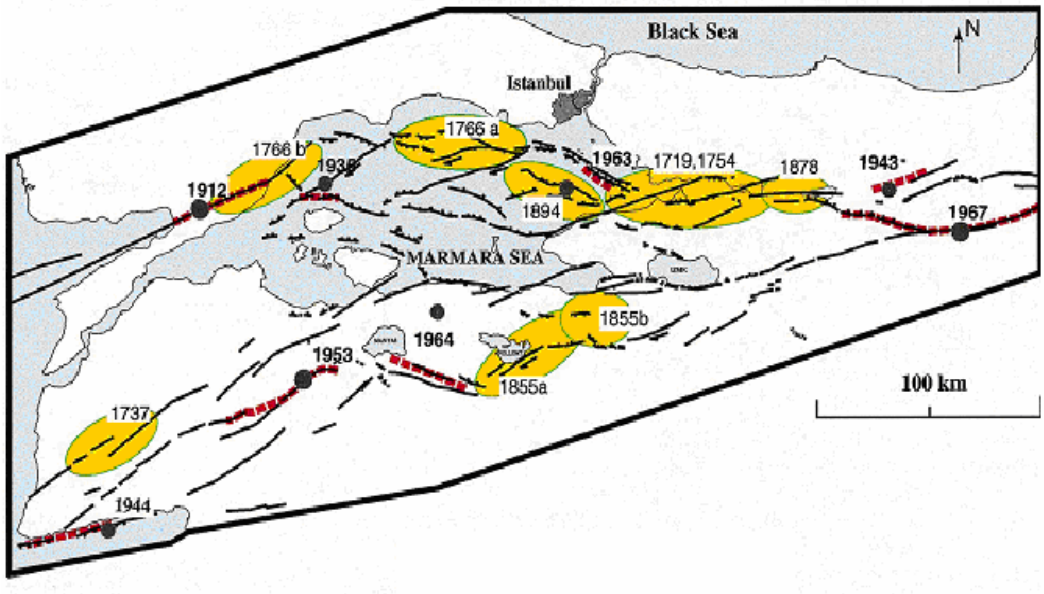

Figure 2.3. Active faulting and historical earthquakes in the Marmara region (modified after Barka, 1997). Black thick lines: active faults recognised by geology and geophysics. Red lines: surface ruptures of earthquakes of this century. Yellow ellipses: estimated rupture areas of historical earthquakes within the period 1700 – 1900 AD

After occurance of the two devastating earthquakes, 17 August 1999 in İzmit (Mw=7.4) and 12 November 1999 in Düzce (Mw=7.2), many studies about seismicity in the region is performed. Karabulut *et al*. (2002) realized study about seismicity distribution after the earthquake (17 August 1999). As a result of this study, the occurance of three clusters are observed when the aftershock distribution is taken into account. The first cluster is extending from Izmit Bay to about 35 km west of the Hersek peninsula. In this cluster mechanism of the events is strike-slip and it shows the entrance of the northern branch of the NAF into the eastern Marmara Sea. Second one is located in the Armutlu peninsula. On the peninsula various fault patterns, E-W striking dextral faults of the NAF zone and NW-SE striking normal faults as a consequence of regional extension, are observed. Third is located 5 km southwest of the Tuzla peninsula. Normal faulting and strike-slip faulting are observed at shallow depth and greater depth, respectively. In conclusion, a noteworthy characteristic of the aftershock events are considered in the region with a focal depth of between 1 and 15 km.

The other worthwhile study based on aftershocks of the 1999 İzmit earthquake is realized by Özalaybey *et al*. (2002). A number of significant aftershock clusters occur on the inferred mainshock rupture plane. The spatial and temporal occurance of these clusters show that they are triggered by the complex redistribution of stresses and dynamic strains imposed by the dislocation of the mainshock. The linear and narrow distribution of the aftershocks and the inferred rupture plane of the İzmit earthquake show that the main branch of the NAF is a single 80 km long throughgoing fault to the west of the mainshock epicenter. The focal mechanisms of the events located in the western end of the rupture zone show both strike-slip and normal-faulting mechanisms. Four events located off the Princes Islands indicate similar source mechanisms characterized by right-lateral strike-slip motion and local trend of aftershock distribution. This observation leads to seismotectonic evidence that the nature of northern boundary fault, which is known to be a transtensional feature at the surface, is dominated by strike slip motion at depth. This dominant feature in the fault zone shows consistency for seisimicity studies in the region.

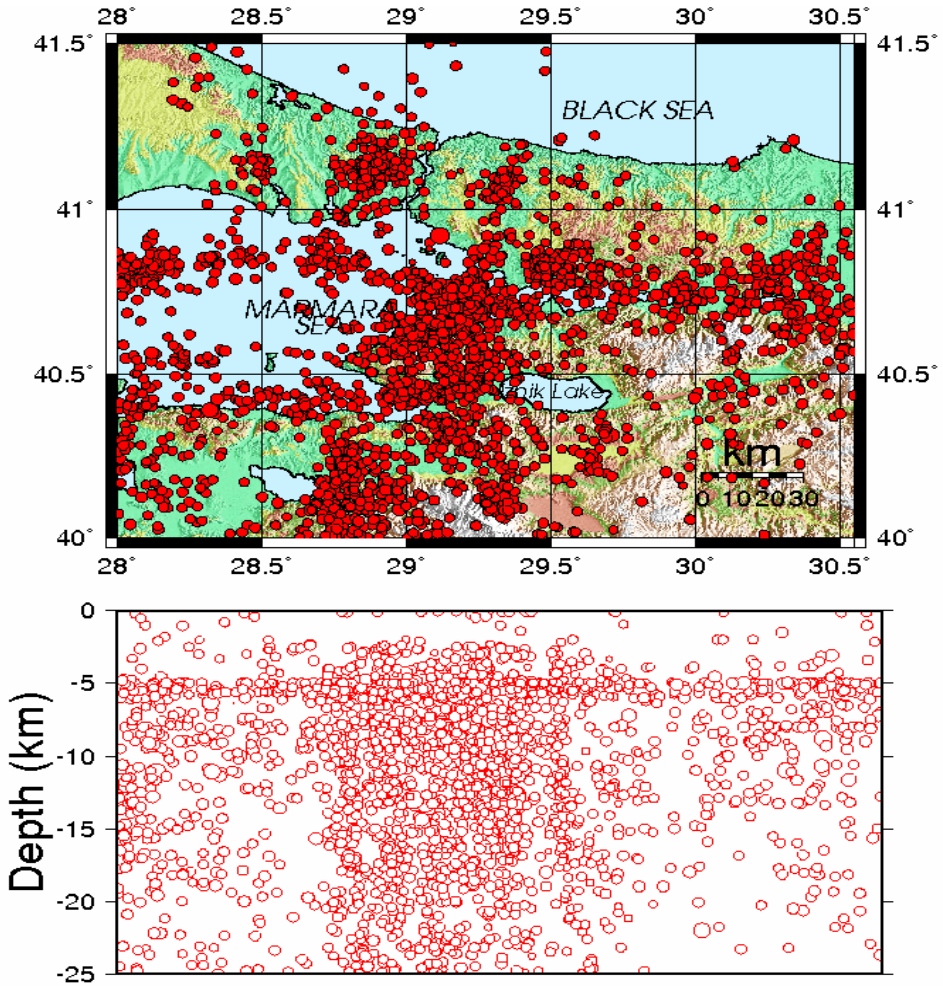

Figure 2.4. Distribution of seismicity in the study region between 2000 and 2007 years (KOERI and TUBITAK Catalog)

To observe the recent seismicity distribution in the study region, seismicity map is prepared (Figure 2.4). Events, which are located in study area in between 40-41.5 N and 28-30.5 E geographical coordinates, are selected since 2000 till end of 2007. Occured events have local magnitudes between 1.5 and 4.2 in the study region. Linearity along the northern strand of the NAF is still continuing and main cluster is observed between 28.7 E and 29.7 E and main seismic activity occurs at the depth range between 5 and 15 km.

2.4. Previous Studies in the Region

Marmara is one of the tectonically most active region in Turkey. Many important earthquakes occured in the region when the history of seismicity is searched. Generally, earthquakes which have the large magnitudes occured western part of the fault zone. This activity attracts the scientist to reveal the crustal properties and apply different geophysical methods to study about the fault zone and the region. Multidisciplinary observations before, during and after the Izmit earthquake in the western part of the NAFZ was made by Honkura *et al*. (2000). They focused on distribution of fault slip, seismicity in the region through using local events before the mainshock, hypocenter of the mainshock and distribution of aftershocks. To extract the resistivity structure along a profile which cross through the north and south branches of NAF, magnetotelluric measurements were taken. The resistivity is very low, less than $10\,\Omega\,\mathrm{m}$, below the northern branch to a depth of $10\,\mathrm{km}$. A high resistivity zone exists below the low resistivity zone.

To investigate the deep electrical resistivity structure of the fault rupture area for the Izmit earthquakes, Tank *et al*. (2005) acquired magnetotelluric data along two profiles crossing the western part of the NAFZ. Conclusions of this study implies the hypocenters of the mainshock and aftershocks are located on highly resistive side and a low resistivity zone extending down to 50 km between the two fault branches. Additionally, 2-D modelling are done and horizontal and vertical cross sections were obtained. A shallow low resistive zone reflecting young sediments (0-5 km depth), a high resistivity zone where the hypocenters of the Izmit earthquake and aftershocks are located (5-15 km depth) and other low resistive zone that corresponds to a region where postseismic creeping takes place (>15 km depth) are properties of three layers when models are examined horizontally. On the other hand, three different sections are observed when models are examined vertically. From south to the north a high resistive zone representing south strand of the NAFZ, a low resistive collision zone between the two branch of the NAF and a high resistive zone represent the northern strand of NAFZ appear. In conclusion, earthquakes tend to occur mostly in a high resistive zone underlain by low resistive area. This low resistivity area is a fluid rich region where the fluid supply is the parital melting process occuring at a deeper conductor. Postseismic creeping is originated from the fluid rich region which triggers the earthquake generation.

Earthquake and controlled source data have been used to observe seismic velocity variations in the Marmara region. Crampin and Üçer (1975) investigated seismic velocities beneath the Marmara region by examining 4 earthqaukes recorded at 35 seismic stations. Gürbüz *et al*. (1980) used a quarry blast recordings along a profile between Adapazarı and Bilecik, they observed that the total crustal thickness 28 km around Adapazarı, P wave velocity 5.4 km in the uppermost part of the crust and 8.1 km/s at the Moho discontinuity. Another quarry blast data were analysed in Anadolu Kavağı and the crustal thickness was found 27 km beneath here (Gürbüz and Üçer, 1985). Gürbüz *et al*. (1991) derived P and S wave velocity models for the Marmara Region using earthquake travel time data of seismic stations. The P wave data indicated two velocity discontinuities at the intermediate depths in the crust. The average velocities in the crust and beneath the Moho was 4.5, 5.6, 6.2, and 7.9 km/s and the average crustal structure in the region was 31 km.

To study crustal structure of the eastern Marmara region, Zor *et al*. (2006) applied the receiver function method. The average crustal thickness for the eastern Marmara region was around the 31 km. and they observed that the crustal thickening from west (29-32 km) to east (34-45 km) along the NAFZ in contrast to no significant crustal thickness changes for western part of the region from north to south while crossing the NAFZ. Additionaly, crustal thickening from 29 to 35 km towards the easternmost stations indicate that the crustal structure shows a transitional tectonic regime. Eventually, Zor *et al*. (2006) conclude that the eastern Marmara region seems to be a transition zone between the Marmara Sea extensional domain and the continental Anatolian inland region.

Recently, Bekler *et al*. (2008) made seismic refraction survey in order to investigate crustal structure beneath the eastern Marmara region. Two reversed profiles across two strands of the NAFZ were recorded in the Armutlu Highland. Land explosions and quarry blasts are used as seismic sources in this study. A high velocity anomaly (5.6-5.8 km/s) in the central highland of Armutlu block and the low velocity (4.90 km/s) pattern North of Iznik Lake are the two dominant features. The crustal thickness is about 27 km in the North and increases to about 33 km beneath the central Armutlu block in the south. P wave velocities are about 3.95 km/s to 4.70 km/s for the depth range between about 1 km and 5 km in the upper crust.

The other significant approach to reveal crustal structure in the region is tomography studies. Karabulut *et al*. (2003) applied 2-D traveltime tomography via using seismic refraction data along 120 km profile from Şile to Gemlik which is crossing the NAF. Low velocity zones on the North and South branch of the NAF was observed. Imaging the 3-D P wave velocity structure in and around the focal area of the 1999 İzmit earthquake (Mw=7.4), Nakamura *et al*., (2002) has been made the tomographic inversion. In this study, 1999 İzmit earthquake and aftershocks were used. Aftershocks are observed a 170 km long narrow zone in an east – west direction along the northern branch of the NAFZ. They mainly distributed three points in the region; near the hypocenter of the mainshock, near 29.2° E in the Marmara sea, and the east of 30.4° E. The P wave velocity structure obtained has a distinct low velocity area to the mainshock hypocenter and the high velocity anomaly is observed the shallower depth of the southern branch (Iznik – Mekece fault) of NAFZ. The mainshock hypocenter is located in high velocity region compared with the surrounding areas. Another low velocity anomaly spreads in a wide area west of the mainshock hypocenter at depths shallower than 15 km (Figure 2.5). Barış *et al*. (2005) applied 3-D seismic tomography to arrival time data during 18 years from 1985 to 2002. Strong lateral heterogeneity was observed at the western part of the NAFZ and similar observation was made about the hypocenter location of the İzmit earthquake as like the other tomography studies.

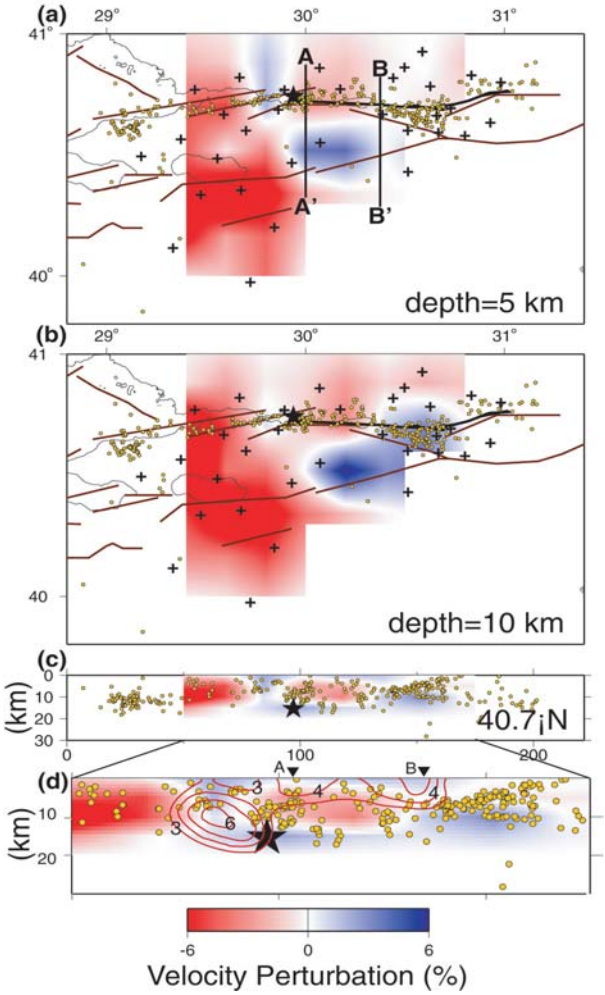

Figure 2.5. Tomographic image shows the plan views at different depths and east – west vertical cross section and the bottom is the magnified of the cross section. Blue and red shading represents the high and low velocity from the initial velocity model. Yellow circles show the relocated aftershock hypocenters and seismic stations used (crosses) are also shown (Nakamura *et al*., 2002)

3. METHODOLOGY

Forward and inverse modellings are instruments for mathematical interpretation of geophysical data. Several attempted models are tested by comparing their theoretically expected results with the actual data in forward modelling. The model that best fits the data is then chosen. Modelling requires a knowledge based on a physical law, convenient process to make a computation, and realise of the geological limitations. Alternatively, inverse methods can be used to derive an optimal solution from the geophysical data when internal consistency of the data and resolution are taken into consideration.

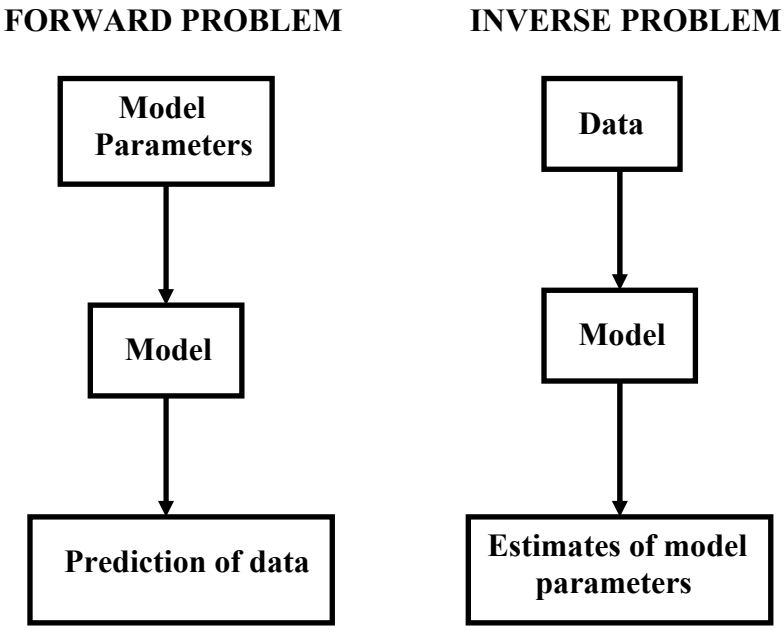

Figure 3.1. Flow diagram of forward problem and inverse problem

The term " inverse theory " is used in contrast to " forward theory " which is defined as the process of predicting the results of measurements on the basis of model. Inverse theory helps us to provide information about unknown numerical parameters that go into the model, not to provide the model itself (Menke, 1984). In many inversion techniques, least square inversion is the most preferable algorithm. Least squares inversion finds application in a wide variety of geophysical problems on account of its mathematical

exactitude. Least squares methods generally easier to solve the “forward problem” that transforms a set of model parameters into a synthetic data set, then to proceed in the opposite direction and solve the inverse problem. Least squares method is implemented to fit of the data through appropriate model parameters. This means that prefered model concured the data under absolute limitations. Association between the model response and the model parameters cause to solve inverse problem in terms of linear or nonlinear sense.

3.1. Linear Least Square Inversion

If the model response *f* is a linear function of the parameters, a perturbation of the model response is represented in matrix notation,

$$f = f^0 + Z\delta \tag{3.1}$$

where $\mathbf{f}^{\mathbf{0}}$ is the initial model response and **Z** is Jacobian matrix of partial derivatives with elements of model function and model response.

$$Z_{ij} = \frac{\partial f_i}{\partial \theta_j} \tag{3.2}$$

Our choice of perturbation in model response will be made so as to minimize the sum of squares of the errors between the model response and the data (Lines and Treitel, 1983). Let **e** represent the error vector expressing the difference between the model response **f** and the observed data **y**.

$$y - f = e \tag{3.3}$$

Combining (3.1) and (3.3) yields

$$y - f^0 = Z\delta + e \tag{3.4}$$

The discrepancy vector **g** contains the differences between the initial model response and the observed data.

$$g = y - f^0 \text{ and } e = g - Z\delta \tag{3.5}$$

Geophysical inverse problems are generally not well posed, the Jacobian matrix **Z** is not square and of full rank. These problems are defined as overdetermined that is, the number data is more than the number of model parameters. In the case of deficiency, damped least square methods alleviate the problem and help to solve inverse problem (Lines and Treitel, 1983).

The basis of least squares approach is estimating the parameter change vector δ and minimizing the cumulative squared error $S = e^T e$ with respect to the parameter change δ. If we substitute equation (3.5) into *S*, we obtain

$$S = e^T e = (g - Z\delta)^T (g - Z\delta) \tag{3.6}$$

Minimization of **S** with respect to δ requires that

$$\frac{\partial S}{\partial \delta} = 0 \tag{3.7}$$

Substituting (3.6) into (3.7) gives

$$\frac{\partial}{\partial \delta}(\delta^T Z^T Z\delta - g^T Z\delta - \delta^T Z^T g + g^T g) = 0 \tag{3.8}$$

Carrying out the differentiation with respect to δ , we obtain “normal equations”

$$Z^T Z\delta = Z^T g \tag{3.9}$$

whose solution for the parameter change vector δ is

$$\delta = (Z^T Z)^{-1} Z^T g \tag{3.10}$$

3.2. Damped Least Squares Inversion

An alternative least squares method, that is "Damped Least Squares Inversion", is using to reduce the difficulties when the matrix $Z^T Z$ is nearly singular. In this case the constraining condition that the sum of squares, or energy of the elements of the parameter change vector δ is imposed and it is bounded by a finite quantity, δ_0^2 (Lines and Treitel, 1983). Thus δ is choosen to minimize a cost function $S(\delta, \beta)$,

$$S(\delta, \beta) = e^T e + \beta(\delta^T \delta - \delta_0^2) \tag{3.11}$$

where β is a damping parameter.

Differentiation with respect to the vector δ yields a modified form of the normal equations

$$(Z^T Z + \beta I)\delta = Z^T g, \tag{3.12}$$

so that

$$\delta = (Z^T Z + \beta I)^{-1} Z^T g \tag{3.13}$$

Comparison of (3.10) and (3.13) denotes that the constraint has produced a method for avoiding singularities or near singularities in the matrix $Z^T Z$. Damping parameter β is added the main diagonal of $Z^T Z$, it damps out changes in the parameter vector θ by limiting the energy in the parameter discrepancy vector δ. This nonlinear inversion approach iteratively update the parameter vector for a given geophysical model. The parameter changes from the initial response estimates are determined by use of the

fundamental relation (3.13). An updated parameters which are then used to compute a new model response estimate are obtained. At each stage, the sum of the squares of the error between the model response and the observation values is monitored. The iterative search for parameter estimates terminates whenever either the squared error or a relative change in the squared error become less than a prespecified value. After these convergence criteria have been satisfied, the estimated geophysical parameters have produced a model which has matched the data within our specifications (Lines and Treitel, 1983).

3.3. Seismic Tomography

Seismic tomography is a process to image Earth's interior. It uses a technique based on studying the internal lateral inhomogeneities in the Earth. The basic principle behind seismic tomography is that contributions to the travel time residual arise from different parts of the ray path. If many paths pass through the each section of the Earth but overall paths differ, it may be possible to isolate the regions in which the travel time anomaly arises. This aim easily complemented by gridding the Earth into cells and the examining the many ray paths that travel through them. By representing the medium as a grid, a forward velocity model is constructed to estimate the travel-time and the refraction path of each ray. By propagating a finite difference wavefront across the grid from a known source location, the travel-times can be estimated. Differences between the estimates and the measured travel times are used to iteratively update the velocity grid from each receiver to the source. The process is repeated a specific number of times, or until no noticeable changes occur.

Tomographic methods usually involve some sort of iterative algorithm to invert the traveltimes (Dines and Lytle, 1979; Peterson *et al*., 1985). A problem with these techniques is a tradeoff between resolution and stability of the solution. At some point, as one attempts to see smaller features, the inversion becomes unstable and velocity artifacts appear. Velocity artifacts are seen as fluctuations of values between adjacent points and the smearing of anomalous zones. Therefore, too few iterations will produce an image which lacks detail, and too many will overfit the data, and produce an image with an abundance of artifacts. A cross-validation method can determine the number of iterations needed (Peterson and Davey, 1990). Also, this method can give a way to determine several

solutions to a non-unique problem, which can be then averaged to produce an image that may be an improvement over a single solution obtained using all the data at once.

Seismic tomography is studied with the image reconstruction methods based on ray theory to image Earth's interior. Generally, the transform methods and the series expansion methods are used as image reconstruction techniques.

3.3.1. Transform Methods

Transform methods are very limiting as far as seismic imaging problems are concerned since straight raypath propagation and full-scan aperture are generally assumed. However, the transform methods make an excellent introduction to the principles of seismic tomography because of their simplicity and serve as a bridge between applications of tomography in other fields with applications in seismology. The projection slice theorem provides theoretical foundation for the transform methods. Then, another transform method is derived from the projection slice theorem: backprojection ray tomography.

3.3.1.1. Projection Slice Theorem

The projection slice theorem requires that observations of propagating energy be taken along a given projection which is perpendicular to the raypaths. A typical model function used in seismic tomography is the reciprocal compressional-wave velocity, or slowness, which has a direct influence on observed traveltime of the propagated energy. The 2-D Fourier transform of a model function produces the amplitude spectrum. The amplitude spectrum from the 1-D Fourier transform of the data function represents a slice of the amplitude spectrum in the plane. In other words, the 1-D Fourier transform of the projection represented by the data function is equal to on slice of the 2-D Fourier transform of the model function. As is understood, the projection slice theorem gives only one slice of the model function per projection.

3.3.1.2. Backprojection Method

Backprojection technique requires no matrix inversion and can treat a large number of unknown parameters, which are necessary for the tomography study with many blocks or grids. In backprojection method, computation of the model function from the data function is different from the projection slice theorem. The model function represents the unknown parameter such as seismic wave slowness. Experimentally determine the line integral of the model function along each ray which yields set of data functions such as seismic wave traveltime. For each data function, the 1-D Fourier transform is taken and the backprojection method is applied to compute the unknown model function.

3.3.2. Series Expansion Methods

Series expansion methods which modify the model function of the study area easily allowed curved raypath trajectories through the target area and are therefore well suited for applications in seismic tomography. The series expansion methods iteratively update an estimated model function so that it converges toward a true model function with a predicted data function. Two other more accurate but iterative methods are known as ART (Algebraic Reconstruction Technique) and SIRT (Simultaneous Iterative Reconstruction Technique). Their basic theory originates from the series expansion approach. To solve the nonlinear problem in practice estimated ray path lengths are computed using the estimated slowness in the model function and the estimated ray path lengths are used in ART or SIRT algorithm. This is called “an iterative linear approach” to solving a nonlinear problem.

3.4. Local Earthquake Tomography

In Local Earthquake Tomography, the study region was modeled through rectangular blocks and a parameter was set for each block to define the perturbation of P wave slowness in the block. On the basis of the reference Earth model, a set of linear equations for the observed first P wave arrival times are formulated by using earthquakes and seismic rays in cells. Local earthquakes’ significant activation of both compressional and shear

waves and their 3-D spatial distribution composes preferable reason to use local earthquakes as sources for determining seismic arrival time in LET.

The body wave travel time from an earthquake *i* to a receiver *j* is expressed using ray theory as a path integral

$$T_{ij} = \int_{source}^{receiver} u ds \tag{3.14}$$

u is the slowness field and *ds* is an element of path length.

$$t_{ij} = \tau_i + T_{ij} \tag{3.15}$$

The equation above gives the arrival times and τ_i is the earthquake origin time. The residual between observed and calculated times is calculated by

$$r_{ij} = t_{ij}^{obs} - t_{ij}^{cal} \tag{3.16}$$

t_{ij}^{obs}: A set of arrival times measured at from seismic stations (picking arrivals)

t_{ij}^{cal}: The calculated arrival times are determined from equations (3.14) and (3.15) using trial hypocenters, origin times and an initial model of the seismic velocity structure (a priori information).

The residual can be interested in the desired perturbation to the hypocenter and velocity structure parameters by a linear approach

$$r_{ij} = \sum_{k=1}^{4} \frac{\partial T_{ij}}{\partial x_k} \Delta x_k + \Delta \tau_i + \int_{source}^{receiver} \delta u ds \tag{3.17}$$

Additionally, adoption of any finite parametrization of the velocity structure, equation (3.17) is written as

$$r_{ij} = \sum_{k=1}^{4} \frac{\partial T_{ij}}{\partial x_k} \Delta x_k + \Delta \tau_i + \sum_{l=1}^{L} \frac{\partial T_{ij}}{\partial m_l} \Delta m_l \tag{3.18}$$

Almost all LET process is originated from the equation above. In this equation, the hypocenter partial derivatives $\partial T_{ij} / \partial x_k$ are proportional to the components of the ray vector times the seismic slowness at source point. The basis theory denotes that the aim of LET is to increase the estimates of the velocity structure and hypocenters by perturbing them in order to reduce some calculation of the residual to the data when these empirical formulas and necessary parameters to solve these equations are taken into account.

One of the important problem in LET is hypocenter and velocity coupling structure. To succed the aim of LET, we need an iterative scheme for solution, as the hypocenter-velocity structure coupling inherent in equation (3.17) can lead to significant nonlinearity. To reduced form of the matrix of all partial derivatives into two smaller matrices, one containing the hypocenter location information and one containing model parameter information (Pavlis and Booker, 1980; Spencer and Gubbins, 1980; Rodi *et al*., 1981), the complete system of simultaneous inversion equations can be written in the form

$$r = H\Delta h + M\Delta m \tag{3.19}$$

r is the residual vector, **H** and Δ***h*** are the matrix and vector of hypocenter parameter partial derivatives and perturbations, respectively, **M** and Δ***m*** are the matrix and vector of velocity parameter partial derivatives and perturbations, respectively. For the *i*th event,

$$r_i = H_i \Delta h_i + M_i \Delta m \tag{3.20}$$

the set of equations are obtained.

Neglecting the effect of velocity parameters in equation (3.20) while locating the earthquakes has the potential to introduce systematic errors into the estimated hypocenter locations (Thurber, 1992; Eberhart-Philips and Michael, 1993). Similarly, ignoring of hypocenter parameters in equation (3.20) may result in biased velocity parameters. Tomographic imaging with local earthquake data demands the updating of both hypocenter and velocity parameters. At this point, the parameter seperation which is called the ***QR*** decomposition is applied. The ***QR*** decomposition of $\mathbf{H_i}$ (Lawson and Hanson, 1974),

$$QH_i = \begin{pmatrix} r_{11} & r_{12} & r_{13} & r_{14} \\ 0 & r_{22} & r_{23} & r_{24} \\ 0 & 0 & r_{33} & r_{34} \\ 0 & 0 & 0 & r_{44} \\ 0 & 0 & 0 & 0 \\ \vdots & \vdots & \vdots & \vdots \\ 0 & 0 & 0 & 0 \end{pmatrix} \tag{3.21}$$

Using the partition of **Q** below row 4, known as $\mathbf{Q}_0$, to form the equation

$$Q_0 r_i \equiv r_i^{'} = Q_0 H_i \Delta h_i + Q_0 M_i \Delta m \equiv M_i^{'} \Delta m \tag{3.22}$$

The property that $Q_0 H_i = 0$ is used and equation (3.21) edited in respect of damped least square method to find Δm.

$$\Delta m = \left[\left(M^{'} \right)^T M^{'} + \beta^2 I \right]^{-1} \left(M^{'} \right)^T r^{'} \tag{3.23}$$

The equation (3.23) results in a matrix size fixed by the number of velocity model parameters (Spencer and Gubbins, 1980; Thurber, 1983). Therefore, this method is not subject to an increase in the size of the matrix to be inverted as the number of earthquakes included in the inversion grows. Defining inversion problem as equation (3.23) leads to some disadvantages such as the loss of singular value information, the sensitivity of the solution to the choice of damping value and squarring of the condition number of the matrix to be inverted. After solving the equation (3.23) changes in velocity parameters are

applied velocity model and earthquakes are iteratively relocated with a new velocity model during desired iteration number completed.

The other substantial part of the 3-D tomographic inversion is defining the solution quality which is related to resolution. To determine the solution quality, hitcount, DWS and RDE measures are checked. Ray number is considered in hitcount. If blocks have no rays, resolution will be poor for this block. Hitcount helps us to observe blocks which have low and high resolution. DWS describes the amount of data constraining the velocity at that node. High DWS value expresses the high resolution. In the standard discrete inverse theory approach, in the course of finding the solution to the problem $\mathbf{G}\boldsymbol{m}=\mathbf{d}$, an inverse $\mathbf{G}^{-1}$ is computed. One can then directly determine the matrix of model resolution $\mathbf{R}$ (Thurber, 1993)

$$R = G^{-1}G \tag{3.24}$$

Equation (3.24) is called the resolution matrix. The columns of the resolution matrix show how much the true model is smeared into the various parameters of the inversion model. In tomographic studies, resolution matrix has inummerable compenents. Therefore, diagonal elements in resolution matrix is used to evaluate resolution of the model parameters. RDE, hitcount and DWS are searched to perform reliable evaluation about the resolution estimates.

4. DATA ACQUISITION AND PROCESSING

4.1. Seismic Stations

In this study, earthquake data were mainly provided by KOERI. KOERI has 29 seismic stations, both short period and broadband, in the region. Blue triangles show the seismic stations belong to KOERI in Figure 4.1. From January 2003 to December 2006, three years data set are obtained from 29 seismic stations belong to KOERI. These located events are prepared for VELEST through format conversion and data set quality was checked by running VELEST with a priori initial velocity model before combining new data set obtained between January 2007 and October 2007.

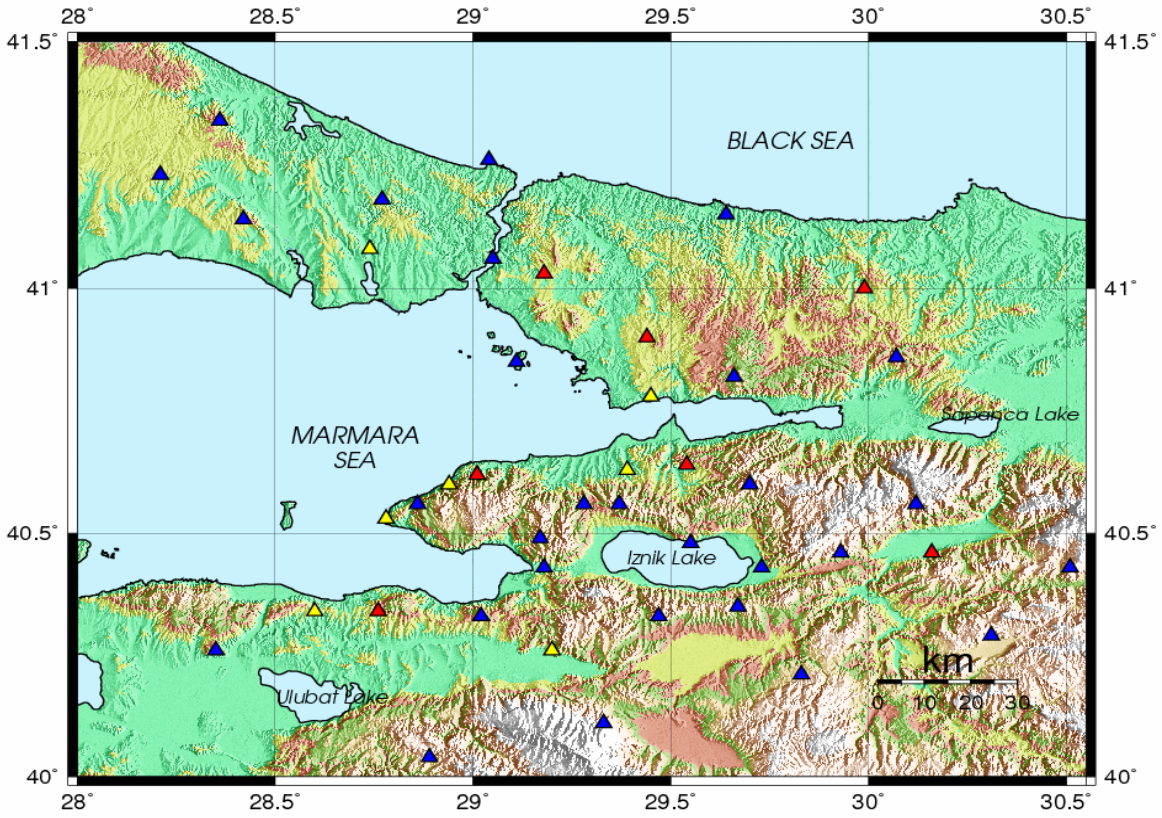

Figure 4.1. Seismic stations in the study area. Blue triangles show KOERI stations, red triangles show temporary stations and yellow stations show TUBITAK stations

To obtain high density station coverage, 7 new broadband stations were installed Site selection for these stations was done according to seismicity distribution since 2001, maximum distance between seismic stations in the existing network and imaging the predetermined places for the purpose of this study. Red triangles show the temporary stations in the region in Figure 4.1. In addition to temporary seismic stations, we obtained data from 7 seismic stations belong to TUBITAK in the study area. Yellow triangles show TUBITAK stations. Data were obtained from temporary, TUBITAK and KOERI stations from January 2007 to October 2007. In total 43 seismic stations were used to provide data from January 2003 to October 2007 for this study.

4.2. Field Experiment

To increase the ray density, 7 broadband stations were installed in the target area. These broadband stations are designed by the Güralp Systems and their model is CMG-6TD. The CMG-6TD is an ultra-lightweight three-component digital output seismometer (Figure 4.2). It uses minimum power, less than 0.9 W at 100 samples/s and it has 24-bit digitizer with GPS unit. To provide the data aquisition seamlessly, solar panel was used to recharge the battery.

Figure 4.2. CMG-6TD with supplied GPS and breakout box

After the site selection procedure, all sensors were tried to installed on basement ground. Configuration of the seismometers was set by using SCREAM. SCREAM is Güralp Systems' major Windows and Linux application for seismometer configuration, real time acquisition and monitoring. Data were recorded at 50 samples/s for the local earthquakes. The system's internal clock is syncronized by the GPS unit to digital converters so that the data were accurately time-stamped to new reference. After starting the data flow, data were collected from temporary stations in two mounts periods.

4.3. Phase Picking

Recorded data were confined from temporary stations using software package which is called SCREAM. Data were copied to an external disk with GCF format in the field. To transfer data to PC from external disk ReadSCSI program was used. Before starting to download data, format conversion was set through ReadSCSI and data were converted to SAC format from GCF format. Obtained data (january,2007-october,2007) from KOERI and TUBITAK stations are also SAC format. Plotting the data set for picking up the arrival times, SAC2000 (Seismic Analysis Code) computer program was used (Figure 4.3).

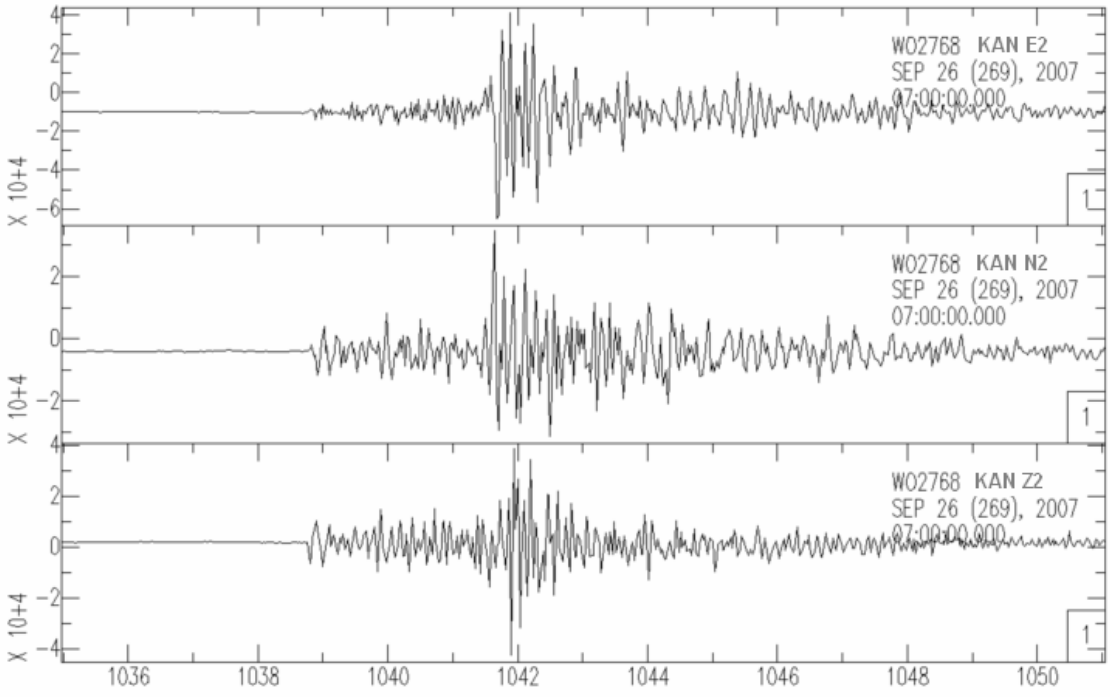

Figure 4.3. An example of the recording at one of the temporary broadband stations

4.4. Earthquake Location

When an earthquake occurs, we observe the times at which the wavefront passes each station. We must find the unknown earthquake source knowing these wave arrival times. The location problem is solved by setting up a system of linear equations for each seismic station. The equations express the difference between the observed arrival times and those calculated from the initial hypocenter and the origin time. We must also have a priori initial velocity model under the network to calculate the travel times of waves from an earthquake at a given depth to a station at a given distance. The system of linear equations is solved by the method of least squares which minimizes the sum of the squares of the differences between the observed and calculated arrival times. The process begins with an initial guessed hypocenter, performs several hypocentral adjustments each found by a least squares solution to the equations, and iterates to a hypocenter that best fits the observed set of wave arrival times at the stations of the network.

HYPO71 locating program (Lee and Lahr, 1975) was used to determine hypocenter of local earthquakes in this study. To find the earthquake location with less error about estimation, a conceivable crustal structure model which defines the study area substantially, exact station coordinates and reliable P and S arrivals are essential.

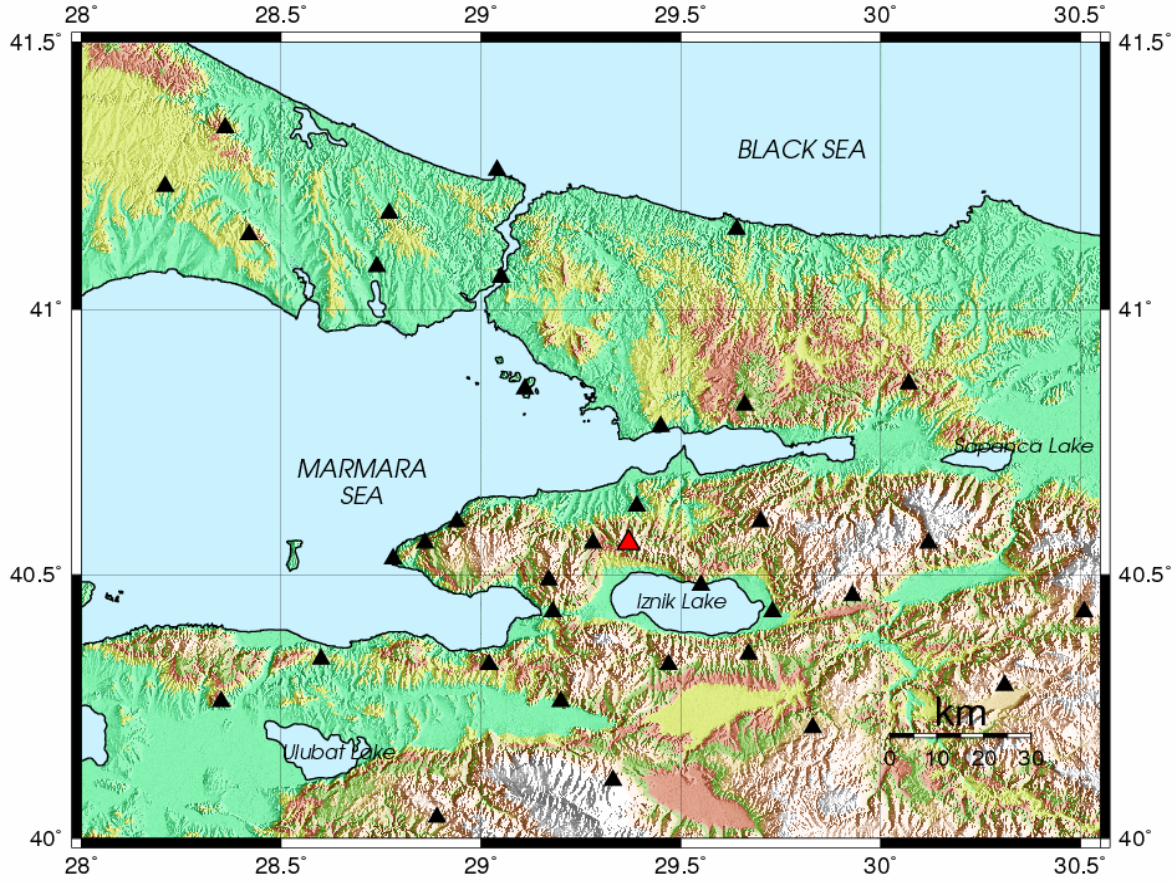

Figure 4.4. Red triangle show reference station in network

After picking the arrival times, data were prepared for HYPO71 input format and velocity model which was modified for VELEST used for earthquake location. In this procedure, YLV is prefered as reference station which is near the center of network with a long recording record and with at least 50% of the total possible readings. For the same reason YLV is used as reference station in VELEST (Figure 4.4). Minimum depth that is the near-surface velocity structure, nearest station distance and farthest station distance are set as considered reference station in network before running HYPO71.

5. MINIMUM 1-D VELOCITY MODEL FOR THE STUDY REGION

5.1. Checking Data Quality

The date range of data set were composed from January, 2003 to October, 2007. After following earthquake location procedure, 640 events were used to obtain minimum 1-D velocity model which will serve as an input to 3-D tomographic inversion. To understand the data quality, VELEST code was run with a priori initial velocity model for the data set. After 9 iterations, obtained outputs were searched and increase in azimuthal gap value was observed for some events. To provide a reliable minimum 1-D velocity model, the best well locatable events in data set were selected and a new data file was created for VELEST. Events were selected based on criteria such as minimum number of observation is 7 for all events, azimuthal gap is less than 180^0, RMS values vary between -0.9 and 0.9 seconds, the relative horizontal and vertical uncertainties of the selected events are less than 2.0 and 3.0 km, respectively. Totally 394 events were selected for 1-D inversion. In this way, the data set was splitted into two data files, the first one with 394 events is for 1-D inversion, the second one with 640 events is for 3-D tomographic inversion but these 640 events will be used again to check quality of solutions using VELEST.

5.2. Calculation of Minimum 1-D Velocity Model

Inversion method tries to fit the available data to ascertain rock property parameters which are consistent with model responses. Therefore, the preference of an acceptable velocity model is crucial for inversion as a forward modelling.

Invention of the 1-D velocity model as initial reference model for seismic tomography, VELEST (Kissling 1988; Kissling *et al*. 1994) computer program was used. Kissling *et al*. (1994) presented to calculate a 1-D model that may serve as reference model for 3-D seismic tomography and for routine earthquake location. Such 1-D velocity models with corresponding station corrections are the result of a simultaneous inversion of a large number of high quality events for both velocity model and hypocentral parameters.

Obtaining an appropriate initial reference model, data are inverted with revised station corrections and hypocenter coordinates. After this procedure, we obtain the minimum 1-D model. Secondly, the 3-D tomographic inversion is designated using minimum 1-D velocity model as the starting model. Before running VELEST, geophysical studies in the region was searched to choose a priori initial velocity model. Various priori initial velocity models were used for VELEST with the same data set for test purposes. Outputs of these runs were studied carefully in terms of average azimuthal gap values and compared changes with station delays and RMS residual errors to perceive a suitable priori velocity model for the study region. In conclusion, priori velocity model for target area pertains a study of crustal structure in the Marmara region using earthquake data performed by Gürbüz *et al*. in 1991. In this study, the data set included arrivals up to a distance of 700 km, origin time errors are less than 1 second, and RMS are less than 0.5 seconds for velocity model.

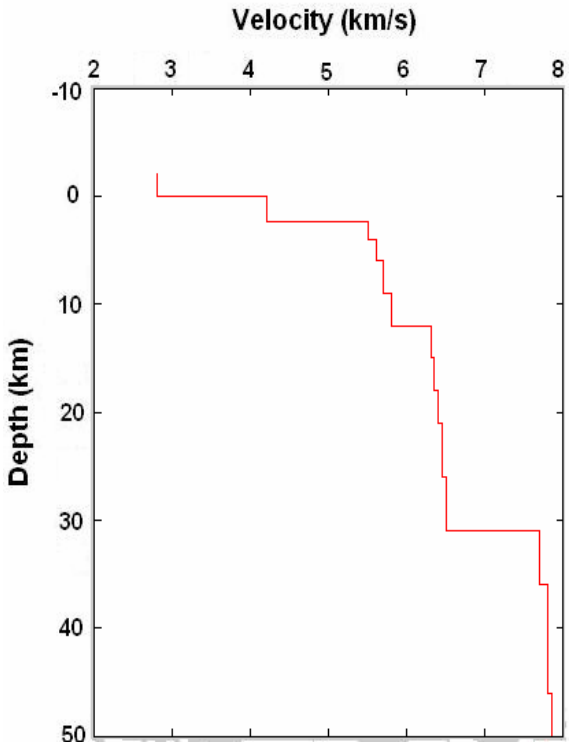

Figure 5.1. Priori initial velocity model (Modified from Gürbüz *et al*., 1991)

Priori initial velocity model has originally four layered earth model. In order to further understand the velocity convergence, additional layers with gradually increasing

velocities with depth were inserted into the initial model. Consequently, 14 layered velocity model was obtained as shown in Figure 5.1. Following 7 iterations, insignificant velocity adjustments and subtle changes in RMS values were observed.

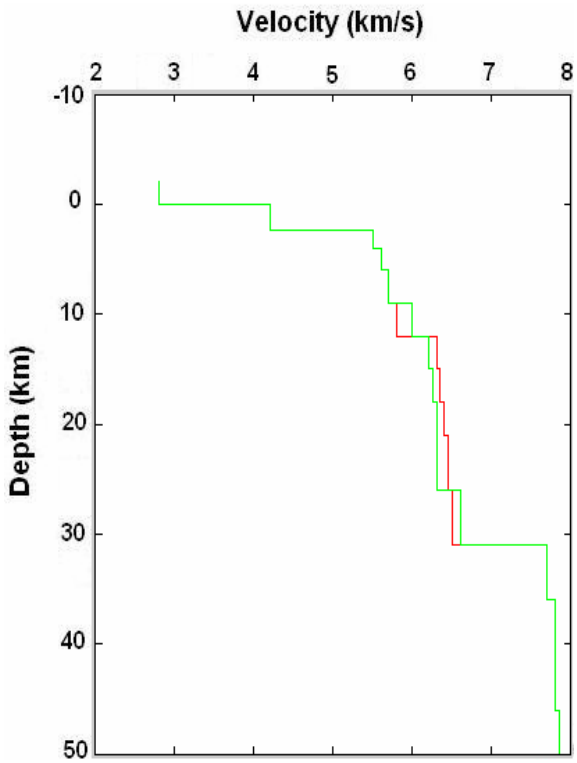

Figure 5.2. Red line shows the priori velocity model and green line shows obtained velocity model after 7 iterations

Figure 5.2 shows priori velocity model and the new velocity model obtained after iterations. Thickness of the first layer and the last two layers were fixed during process. There are not strong contrast between the two velocity models. Only small changes were observed at velocity values. In order to understand the data quality and reveal the reasonable crustal model, the same procedure was repeated with the obtained velocity model.

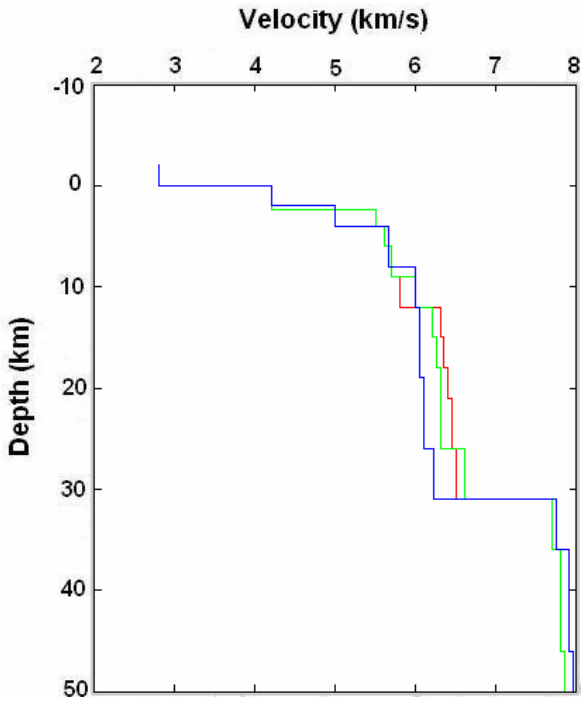

Figure 5.3. Obtained velocity models from VELEST. Red line, green line and blue line shows priori initial velocity models, velocity model as a result of VELEST which is run with priori initial velocity model and potential minimum1-D velocity model, respectively

In this run, VELEST was set for 7 iterations. RMS is reduced to 0.59 seconds for the first iteration and it reached to a minimum RMS value of 0.278 seconds after 3 iterations. Obtained velocity model can be a potential minimum 1-D velocity model for the region. On the other hand, increase of the gap of final epicenters was observed for some events in the data set. These events were eliminated from the data set and 316 events left for obtaining a reliable minimum 1-D velocity model. VELEST was rerun with the new data set and obtained potantial minimum 1-D velocity model. After 7 iterations, new velocity model obtained. It was used as an initial velocity model for 2nd run with the same number of iterations. Figure 5.4 shows minimum 1-D velocity model and priori initial velocity model. For minimum 1-D velocity model, RMS is equal to 0.61 seconds as a result of the first iteration. It reached to a minimum RMS value of 0.288 seconds and average velocity adjustments became stable after 5 iterations, gap values of final epicenters were between 57^0 and 176^0, average azimuthal gap for data set was 114^0 and average final RMS value for data set was 0.24 seconds. Inserted additional layers to the priori initial velocity model

became a single layer which has a constant velocity with increasing depth in minimum 1-D velocity model as a result of inversion.

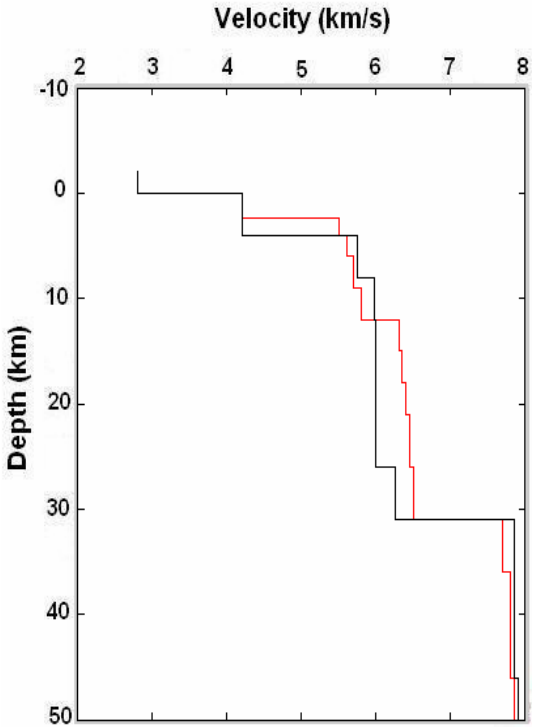

Figure 5.4. Red line and black line shows priori initial velocity model and minimum 1-D velocity model for the study region, respectively

Table 5.1. Minimum 1-D velocity model as a result of inversion

Velocity (km/s)	Depth (km)
2.80	-2.0
4.20	0.0
5.75	4.0
5.97	8.0
6.00	12.0
6.25	26.0
7.85	31.0
7.90	36.0
8.00	46.0

After obtaining minimum 1-D velocity model with well locatable events, the other data set which has 640 events were checked through running VELEST with minimum 1-D velocity model with station corrections in single event option. Output results of the earthquakes were checked. Some events have azimuthal gap bigger than 180^0. RMS values of these events are looked and events which have RMS value bigger than 0.5 seconds were selected for repicking. After data analysis, VELEST was run in single event option for data set again. Decrease in azimuthal gap and RMS values was observed for selected events. Eventually, events which have azimuthal gap was bigger than 180^0 and RMS value was bigger than 0.5 seconds eliminated from the data set. Finally, 560 events were prepared for 3-D tomographic inversion. Defining the range of possible and physical solutions of the minimum 1-D velocity model, unrealistically low and high velocities are used with 560 events. After 7 iterations reasonable convergence are observed for initial and high velocity values (Figure 5.5).

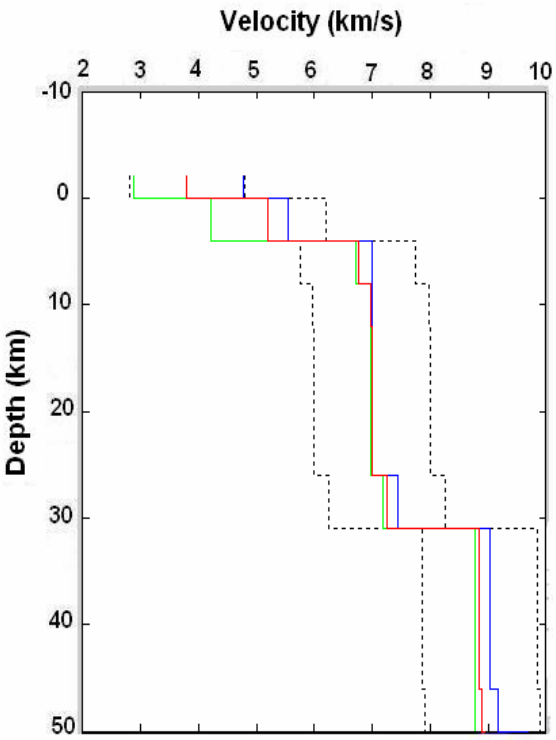

Figure 5.5. Black dashed lines show initial low and high velocity models, red line show minimum 1-D velocity model, green line show output of low velocity model, blue line show output of high velocity model

5.3. Testing Minimum 1-D Velocity Model

5.3.1. Stability

To check the stability of the minimum 1-D velocity model, various tests with randomly and systematically shifted hypocenters were performed. Shifting hypocenters before introducing them in the joint velocity hypocenter inversion, provides a check for a bias in the hypocenter locations and for the stability of the solution to the coupled problem. If the proposed minimum 1-D velocity model denotes a robust minimum in the solution space, no significant changes in velocity and hypocenter locations are expected. Hypocenters randomly (lat, lon, depth) and systematically (depth) by 7 km were shifted before defining in the joint inversion as green dots (Figure 5.6) to check the robustness of the minimum 1-D velocity model. Velocities were overdamped for test with only systematically shifted hypocenters and VELEST was rerun with 5 iterations for random and systematic shifting tests. Hypocenters are relocated close to their original locations showing a stable minimum. Final hypocenters are red dots as shown in Figure 5.6.

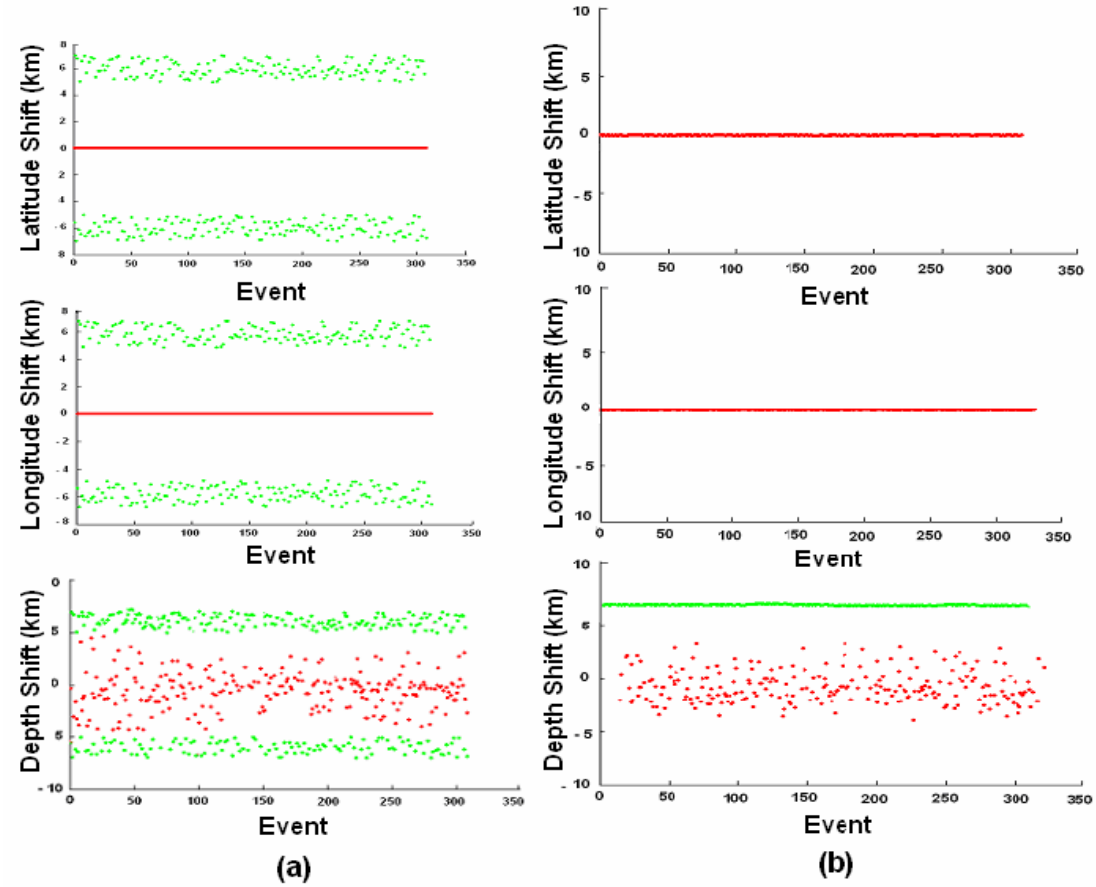

Figure 5.6. (a) Results of random shifting test, (b) Results of systematic shifting test with overdamped velocities

5.3.2. Location Precision

To estimate the absolute location error, quarry blast data were used due to the known source parameters (location and origin time) of the data (Kissling 1988, Kradolfer 1989). Two quarry blast data which has recorded by at least 6 seismic stations were used for this test. Data picked for blast like routine earthquake location procedure. VELEST was run with the minimum 1-D velocity model where the station corrections was fixed. In this test, VELEST was set as a single event option to understand correctness of the minimum 1-D velocity model through comparing obtained locations with true blast locations. Red stars show the true blast locations and blue circles show the locations obtained from VELEST (Figure 5.7). Small variations observed in both latitude and longitude for quarry blast.

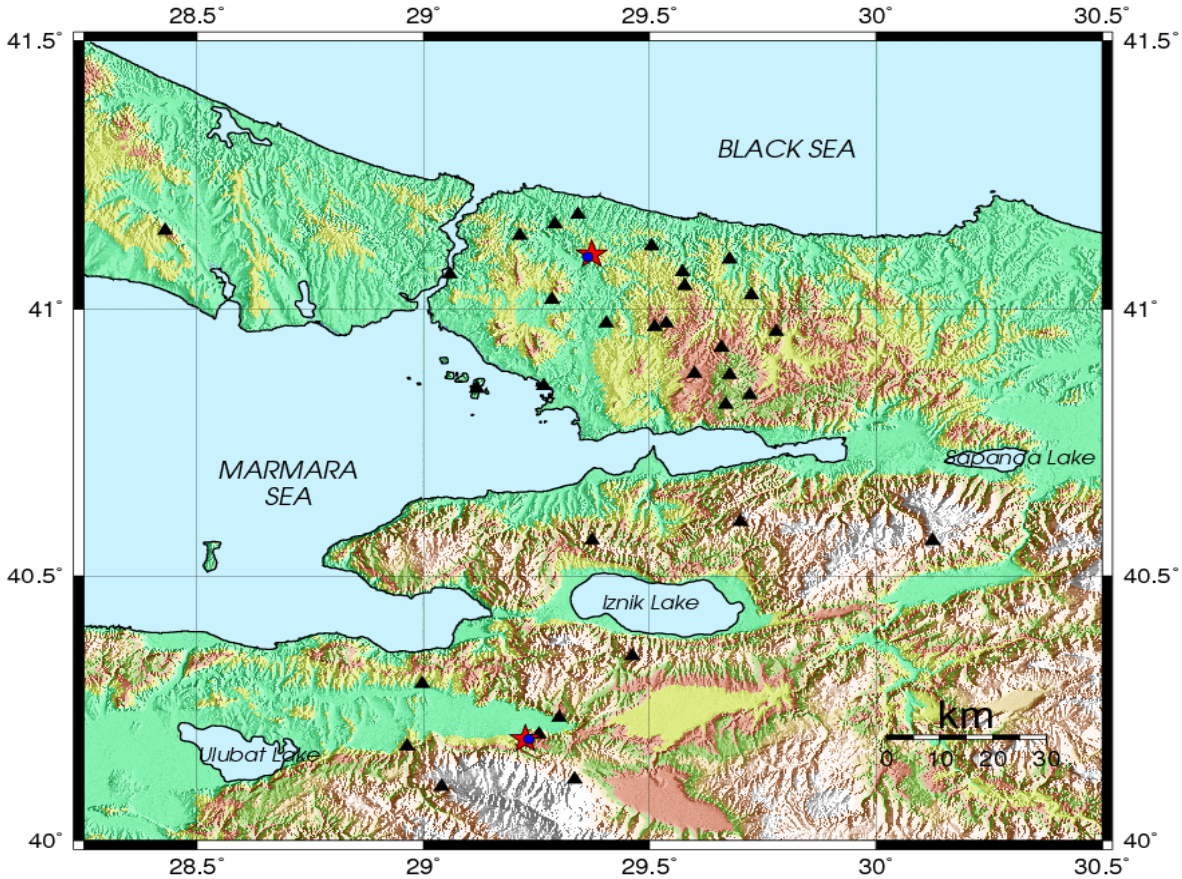

Figure 5.7. Comparison of events locations with the true blasts locations

6. 3-D TOMOGRAPHIC INVERSION

6.1. Introduction

Local earthquake tomography is a process to image 3-D Earth structure from a large set of observations of a targeted Earth volume. The events occur in network borders and should be homogeneously recorded by seismic stations in network configurations.

SIMULPS14 was used as local earthquake tomography algorithm in this study. This algorithm is an extension to the widely used and well tested Simul-code family and it is developed by Thurber (1983) and further developed by Um & Thurber (1987) and Eberhart-Phillips (1986, 1990) among others. SIMULPS14 used damped least square inversion to convert nonlinear problem to linear problem. Damped least square means that the norm of the model perturbations is weighted and combined with the squared data misfit. In this algorithm, P wave reading has a big importance and it composes the main significant step during process because P wave velocity is modeled from P wave arrival times. In this study, targeted area was gridded uniformly when ray coverage and station distribution are taken into account. The most important feature of this code is giving some alternative about the ray tracer. A convenient raytracing method was prefered according to comparison of ray lengths and model parametrization approach.

To display tomographic inversion results, the results should be plotted. In this study, obtained outputs from SIMULPS14 were used as inputs for TOMO2GMT. TOMO2GMT is shareware program and it prepares input in a fashion so that the tomographic results can be easily plotted by GMT. To avoid any additional interpolation by GMT, the results are regridded by TOMO2GMT on a user defined grid using exactly the same type of interpolation as in SIMULPS14.

The main properties of TOMO2GMT is applied within the context of this study. Resolution estimates, model changes and final model values are extracted. For target area horizontal depth slices, vertical depth sections along profiles of constant latitude or longitude and resolution parameters for data set were plotted. All results were tried to comment and associate with the active tectonic and geologic structure in the region.

6.2. Checkerboard Test

Tomographic inversion methods have some questionable parts about the estimation of the reliability of the images or, in other words, knowing how close the image is to the actual structure (Leveque *et al*., 1993). To reveal the images' quality, checkerboard test is applied. In this test, alternating high and low velocity values are assigned to the 3-D grids and the test residual data corresponding to the actual ray paths are computed by 3-D ray tracing in this model. Then these data are inverted and the comparison of the solution with the original checkerboard velocity pattern provides an estimate of the resolving power of the data set.

Before applying the checkerboard tests, target volume was modeled as 8×8, 10×10, 15×15, 20×20 and 25×25 km in horizontal direction. Thicknesses which were calculated from minimum 1-D velocity model were used in vertical direction. Velocity values at the grid nodes were changed as ±10% from the original velocity values. These synthetic models were used as inputs for 3-D tomographic inversion to obtain synthetic data set for all grid spacings. To extract different depth slices, layers which have constant velocities were divided into equivalent sections in minimum 1-D velocity model. After that this velocity model was inserted to SIMULPS14 to rerun with the obtained synthetic data sets for all grid spacings to observe more confidential parts of the velocity changes in the study region.

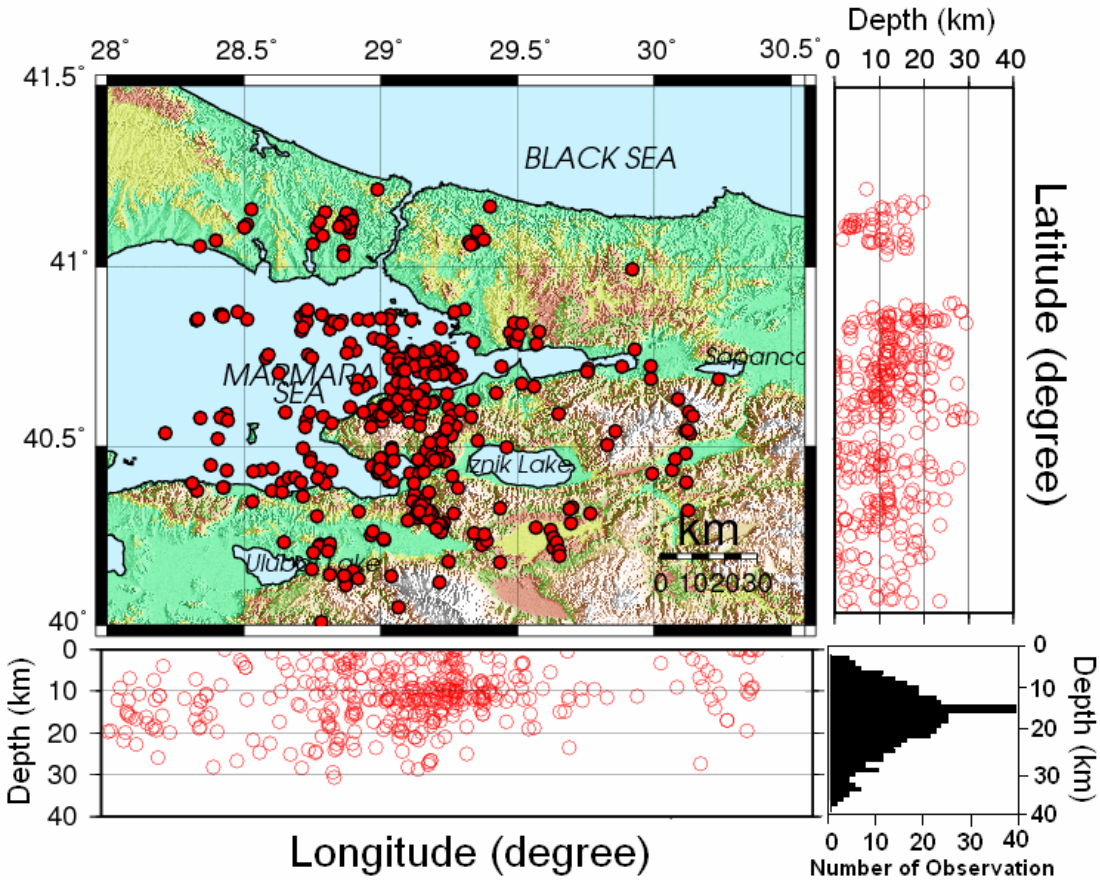

Figure 6.1. Events distribution in Latitude and Longitude with depth distribution histogram

To calculate synthetic travel times, 560 events which have GAP<180^0 and minimum 7 observations were used. In this method, selection of the damping parameter is based on an empirical approach enhanced by Eberhart-Phillips (1986). Single iterative inversions were run with various damping values with the same data set for all cell sizes. After that, the reduction in data variance was compared to model variance. The selected damping parameter was the one which greatly reduced the data variance with a reasonable increase in the model variance as shown in Figures 6.2 and 6.3. Damping values were determined as 10 and 15 for 10×10 km and 15×15 km cell sizes, respectively. Additionally, weighting values were determined for travel time residuals and source-receiver distances. To evaluate entire data set for inversion, maximum values of these weighting factors were assigned. Weighting value was determined as 1 for an epicentral distance 50 km and 0 for distance bigger than 200 km. Values between two distances were weighted linearly. Weighting values for travel time residual were set as 1 for 0.5 seconds, 0 for values bigger than 3

seconds and 0.02 for 1.5 seconds. Weighting for intermediate values was calculated through linear interpolation.

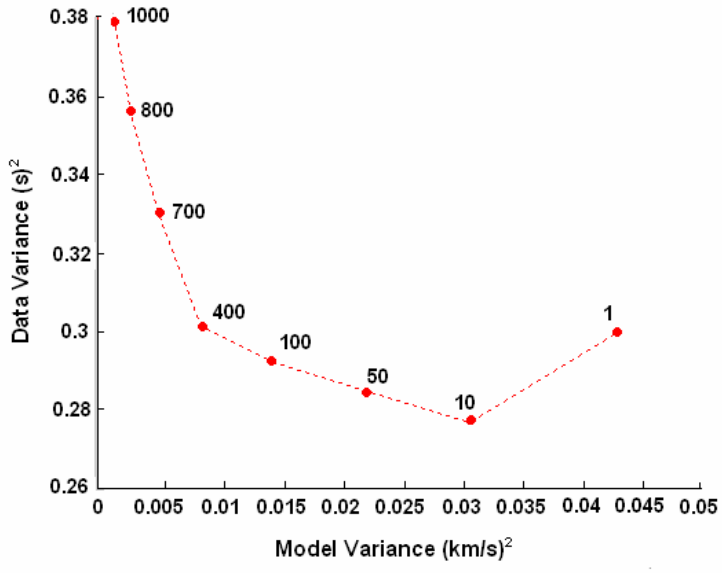

Figure 6.2. The damping curve for 10×10 km cell size. Damping parameter was determined as 10

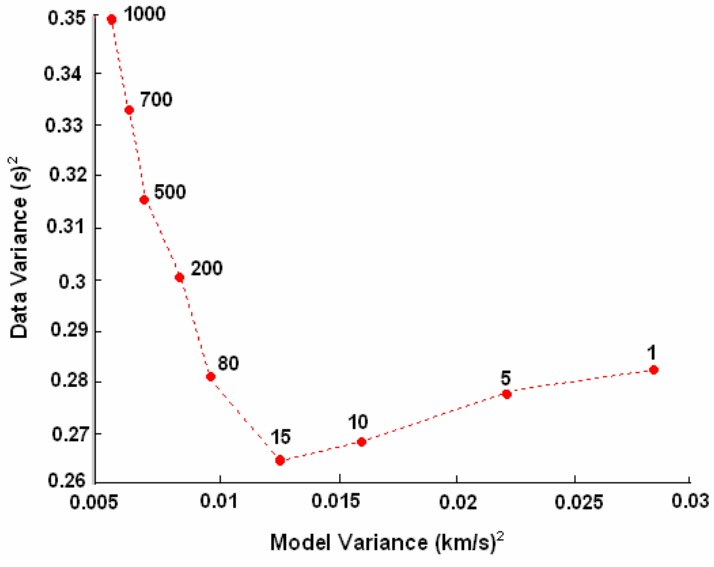

Figure 6.3. The damping curve for 15×15 km cell size. Damping parameter was determined as 15

After 4 iterations, checkerboard test results were obtained. Resolution depends on the number of rays in the blocks. To determine the optimum block size for the best resolution, different cell sizes were used. The 10×10 km and 15×15 km cell sizes denote the high resolving power of the data set compared with the other cell sizes. Figures 6.4 and 6.5 show synthetic models. Figures 6.6 and 6.7 show results of the checkerboard tests. For these two models, resolved number of blocks decreased with the reduced seismicity. Velocities in network borders have a good resolution down to 17 km when the depth distribution of the earthquakes is taken into consideration (Figure 6.1). In Figure 6.6, crustal structure was well resolved between 40.00-41.00 N and 28.00-29.50 E at 17 km, however, the remaining areas were not well resolved because of the depth distribution. On the other hand, a few blocks were resolved for the same horizontal depth section as shown in Figure 6.7, because the number of events were low at 17 km. Also, rays did not cover entire blocks. Eventually, decrease in resolution for the same horizontal depth section was observed for 15×15 km cell size. The other slices at depths 2.4 km, 7.2 km, 12 km denote the same resolving power and resolution quality for the two cell sizes. Consequently, velocity structures were ideal for the results of the checkerboard tests and good resolution was seen in some areas where the high earthquake density was observed.

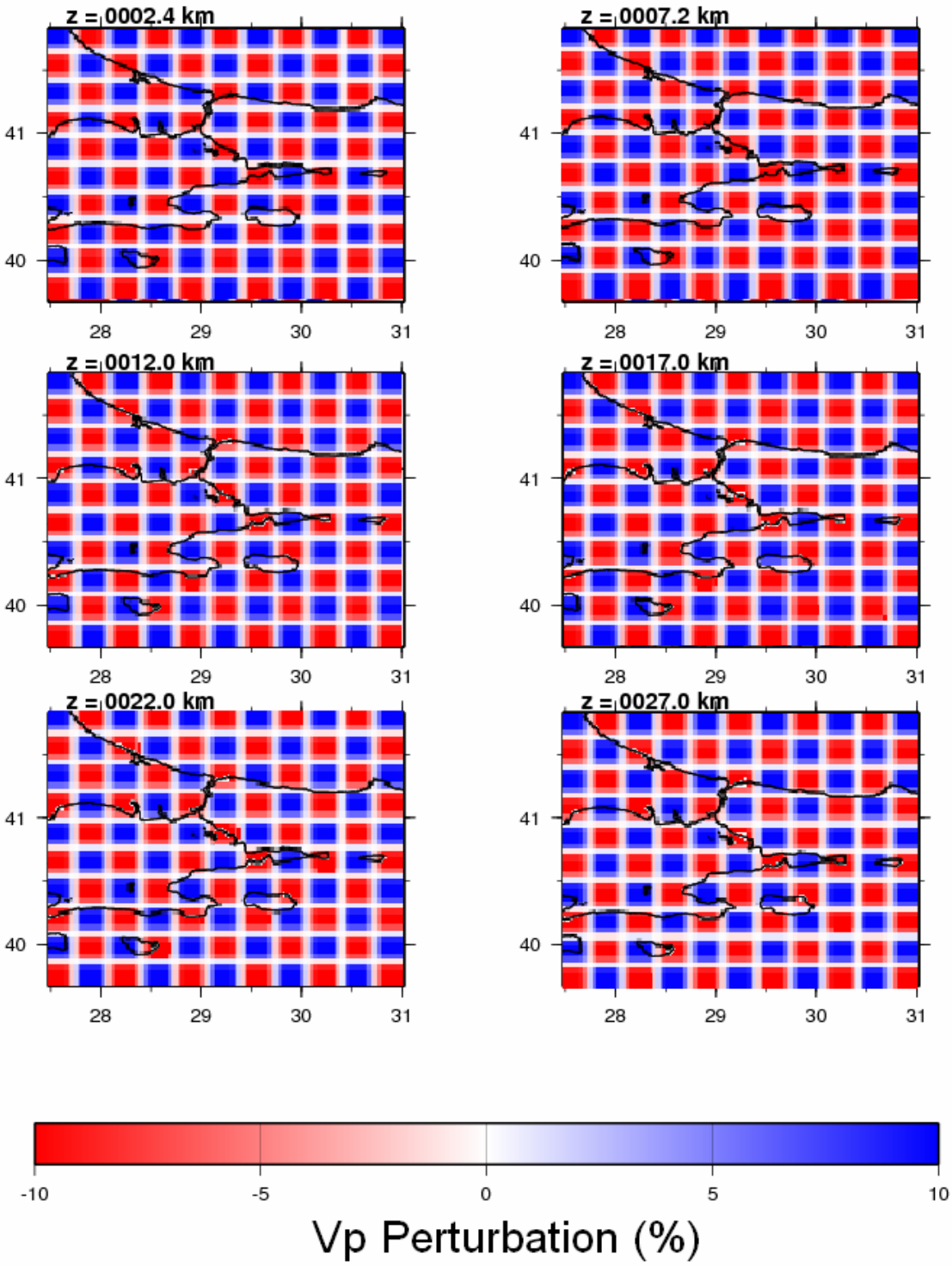

Figure 6.4. Synthetic model for 10×10 km cell size

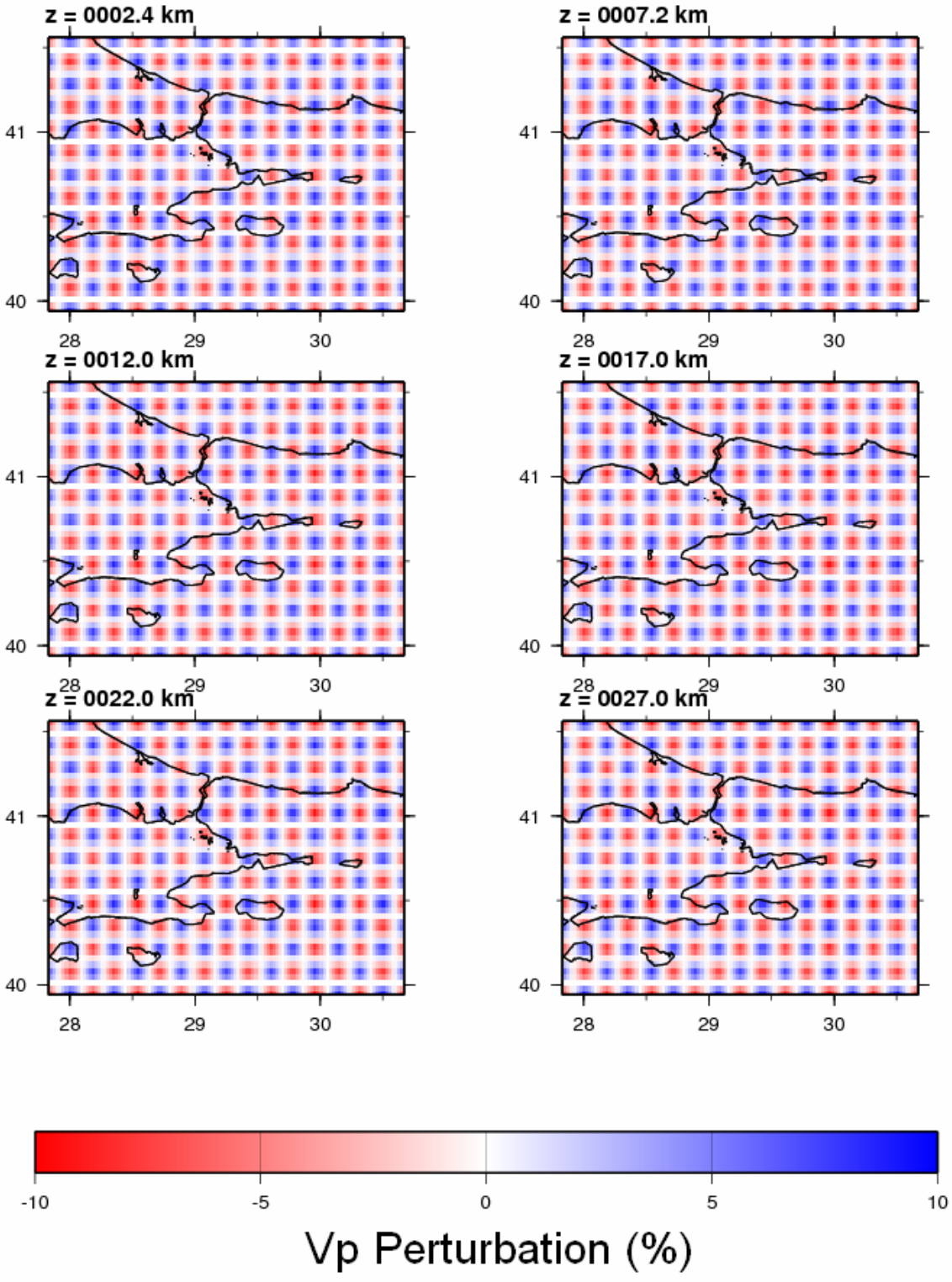

Figure 6.5. Synthetic model for 15×15 km cell size

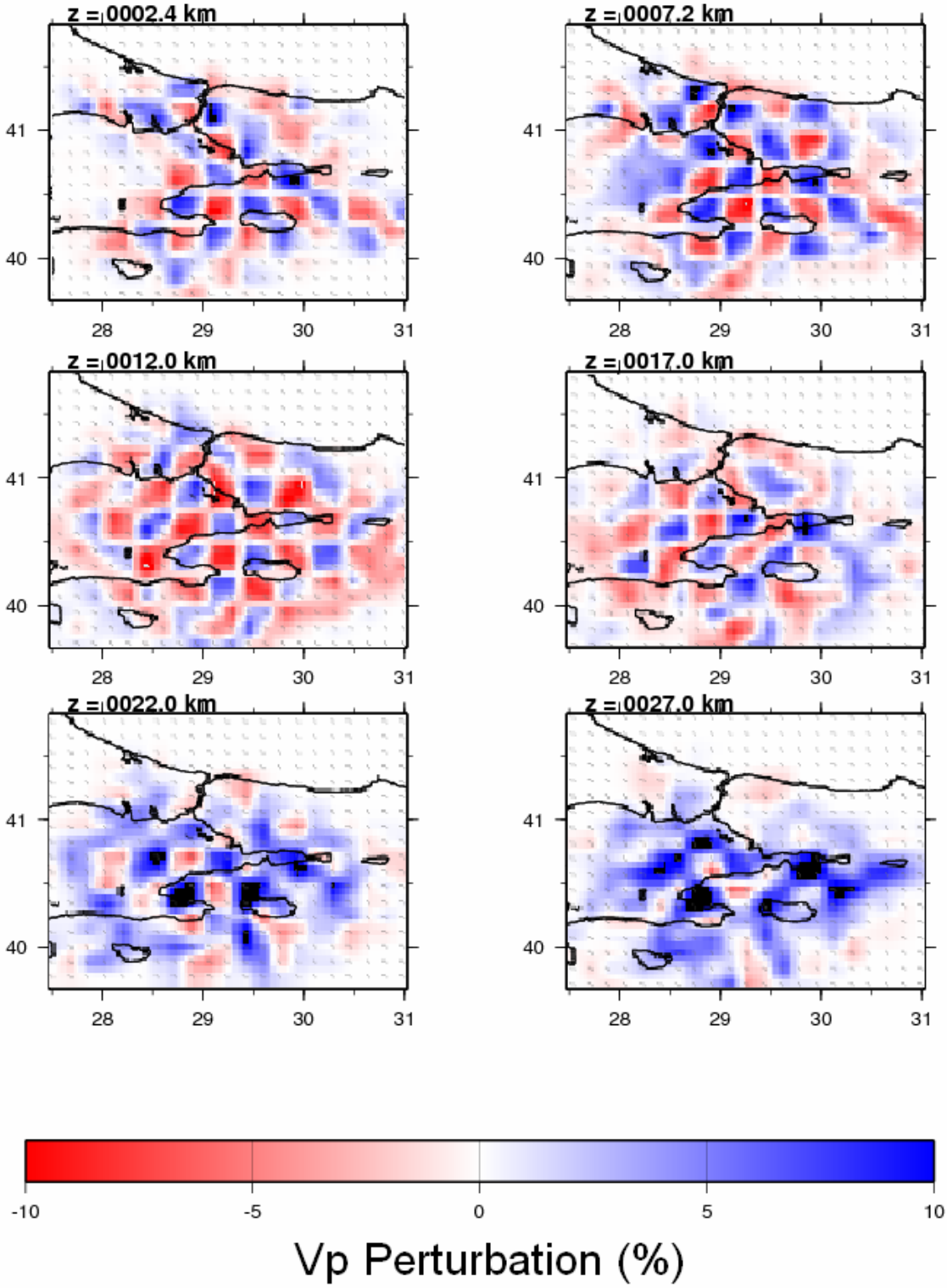

Figure 6.6. Result of the checkerboard test for 10×10 km cell size

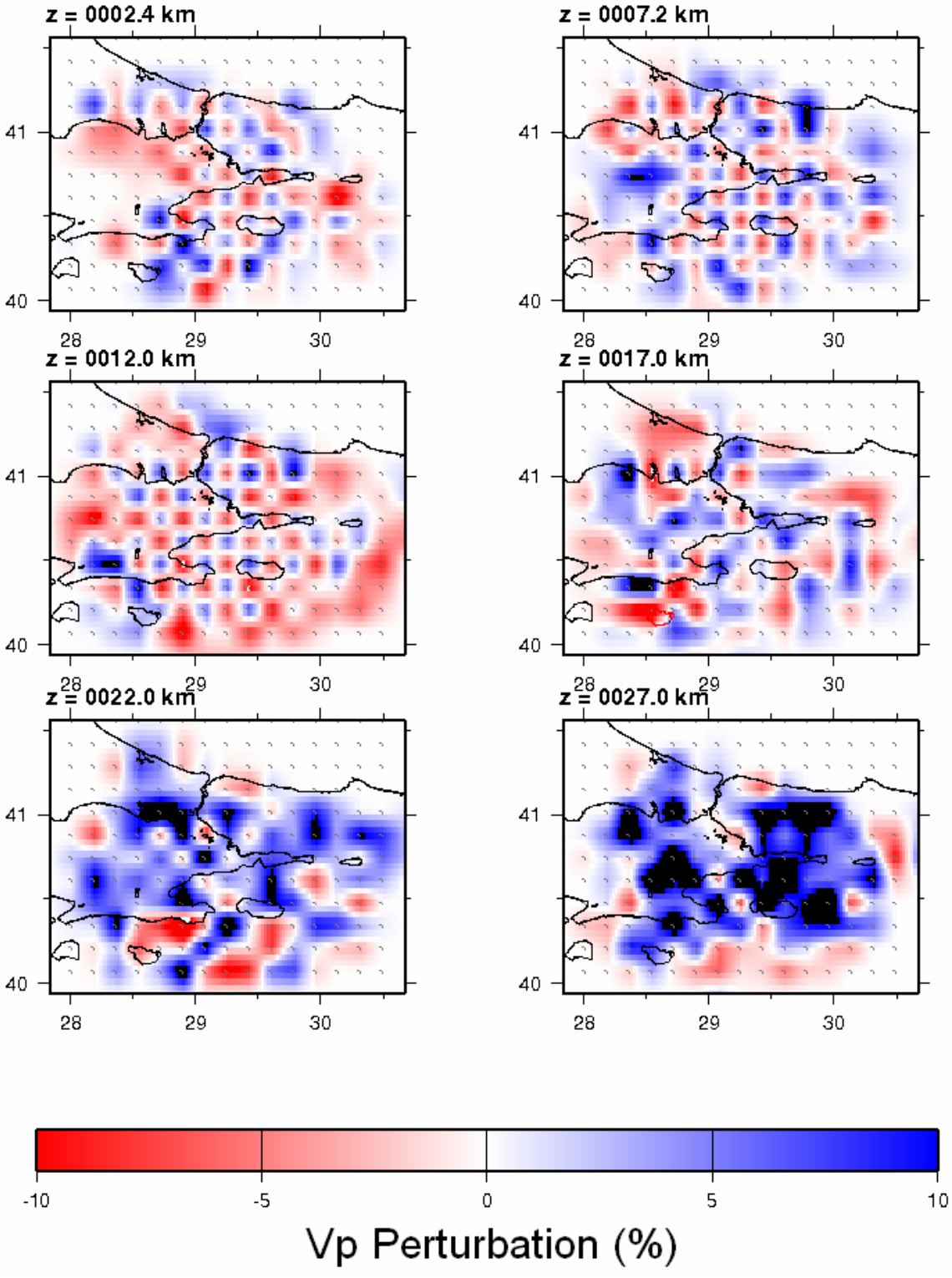

Figure 6.7. Result of the checkerboard test for 15×15 km cell size

6.3. Model Parametrization

In LET studies, there are different ways to represent the Earth's velocity structure. All are just approximations to the true 3-D structure in some part of the Earth. In SIMULPS14, velocity structure represantation is based on a 3-D grid of nodes (Thurber, 1983).

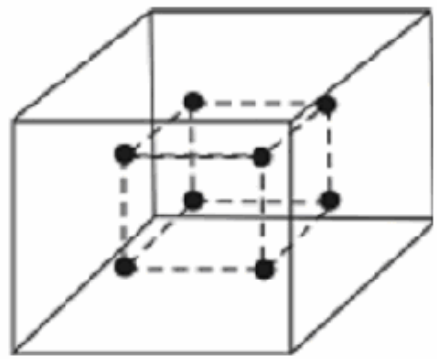

Figure 6.8. Schematic indications of discrete velocity model representations: a grid of nodes. Dashed lines indicate the spatial form of interpolation

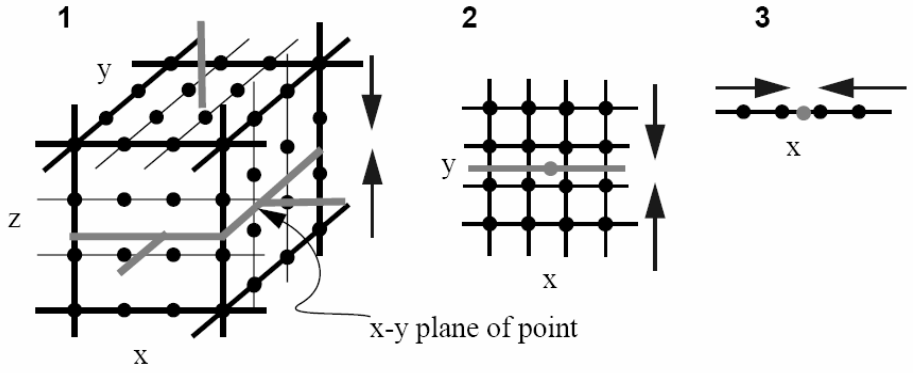

Figure 6.9. Scheme for 3-D cubic B-spline interpolation. The solid black circles are the control values (grid nodes) and the grey circle is the target point. 1) Interpolation along z onto x-y plane of point. 2) Interpolation along y onto x-coordinate of point. 3) Interpolation along onto x-coordinate of point

The other model parametrization techniques use blocks but Thurber adopted grid nodes to model the earth structure. Velocities at the nodes are treated as unknown parameters but their value at any point in the model is calculated by interpolating velocities at eight nodes surrounding that point. Consequently, this model behaves that velocity is continuous everywhere in the model and no velocity discontinuity is allowed to exist even when discontinuities are actually detected in the study area.

Our study region is approximately 210×167 km and it was defined by regular grids. Regular grid spacings were assigned right-left and up-down directions from the coordinates of the center point in the study region for $8 \times 8,\ 10 \times 10,\ 15 \times 15,\ 20 \times 20$ and 25×25 km in horizontal direction. Target area borders exceeded to provide uniformity when regular grid spacing was applied. Outside of the network borders and some blocks which have amount of data less than 7 held fixed during inversion. For vertical direction, thicknesses and velocity values were assinged via using minimum 1-D velocity model.

6.4. Ray Tracing

Ray tracing methods use high frequency approach to solve elastic wave equation. It is used for predicting or determining arrival times of waves at seismic station using raypaths. Ray tracing requires an initial velocity model and the assumption that rays behave according to Snell's law. There are many techniques for determining ray paths and travel times as there are ways of representing the Earth’s structure. To select the most appropriate method to use for calculating raypaths and traveltimes, the form of the represent the 3-D structure and events locations in network configuration are important.

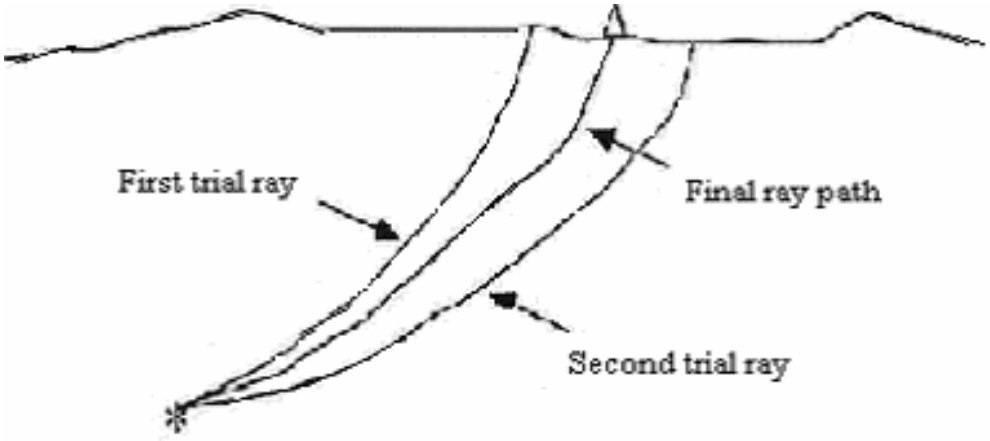

Figure 6.10. Illustration of the shooting method

In this study, shooting method was prefered to use for ray tracing due to the results of accuracy for longer rays exceeding approximately 60 km and our regular grid spacing approach. In shooting method, one point is chosen as an initial point. The rays are shoot from this point under different take-off angles. The initial conditions (starting depth, azimuth, and take-off angle) of the ray were cited and the path of the ray was computed through a given velocity model. An iterative loop is used to detect the ray which passes through the second point.

RKP-ray tracing is a shooting method in SIMULPS14 and it was adopted from a code by J. Viriuex (1991). It uses paraxial rays and perturbation theory. Additionally, RKP-ray tracing requires that velocities are defined on a regular grid and an interpolated in between by 3-D cubic B-splines. In theory, the slowness vector ***p***, the eikonal equation can be cast into Hamiltonian formalism as proposed by Burridge (1976):

$$H(x,p,\tau)=\frac{1}{2}\left[p^2-u^2(x)\right] \tag{6.1}$$

x is the position along the ray and ***τ*** is a sampling parameter along the ray. The eikonal equation implies that *H=0* along a ray and the ray tracing equations are then given by Hamiltons canonical equations

$$\dot{x} = \nabla_p H = p$$
$$\dot{p} = -\nabla_x H = \frac{1}{2}\nabla_x u^2 \qquad (6.2)$$

where ∇_x and ∇_p show the gradients with respect to vectors ***x*** and ***p***, respectively. This system [equation (6.2)] has then to be solved for $x(\tau), p(\tau)$ with the given shooting angles to find the raypath and, by integrating over $p(\tau)$, the traveltime. Shooting normally implies that the initial values (first guess) have to be adjusted so that the ray surfacing point reaches the station with a required accuracy. For these adjustments the concept of paraxial rays proves to be very useful. An already traced ray, described by $x_c(\tau)$ and $p_c(\tau)$, will be called the central ray. Position and slowness of the paraxial ray are then given by

$$x(\tau) = x_c(\tau) + \delta x(\tau)$$
$$p(\tau) = p_c(\tau) + \delta p(\tau) \qquad (6.3)$$

where δx and δp are the perturbations of position and slowness of the central ray. These perturbations have to satisfy the paraxial ray tracing equations, deduced by first order linear perturbation of equation (6.2)

$$\begin{bmatrix} \delta\dot{x} \\ \delta\dot{p} \end{bmatrix} = \begin{bmatrix} \nabla_p \nabla_x H & \nabla_p^2 H \\ -\nabla_x^2 H & \nabla_x \nabla_p H \end{bmatrix} \begin{bmatrix} \delta x \\ \delta p \end{bmatrix} \qquad (6.4)$$

where H and its derivatives are computed on the central ray. Solution of equation (6.4) represents a paraxial ray, the additional constraint of $\delta H = 0$ must be fulfilled. Two paraxial rays, both with $\delta x(0) = 0$, one with $\delta p(0)$ associated with a change in initial azimuth and one with $\delta p(0)$ associated with a change in take-off angle, are necessary to update the shooting angles. Variations in take-off angle and initial azimuth values can be estimated from the conditions of these paraxials at the surface and the distance of the surfacing point of the central ray to the station. The solution of the ray tracing equations (6.2) and (6.4) require the integration of a set of differential equations. A fourth order

Runge-Kutta solver is used in the numerical integration and this ray tracing type is abbreviated as RKP-ray tracing (Runge-Kutta + Perturbation).

6.5. Results of the 3-D Tomographic Inversion

The data set consists of 14329 P wave arrival times from 560 local events recorded at 43 seismic stations covering an area of 210×167 km. To provide reliable data set, events which have azimuthal gap less than 180^0 and recorded at least 7 stations were selected for 3-D tomographic inversion. Projection of the ray path between source and receiver on the earth surface for selected events is shown in Figure 6.11. In light of the computed checkerboard test results, 3-D tomographic inversion was applied for 10×10 and 15×15 km cell sizes.

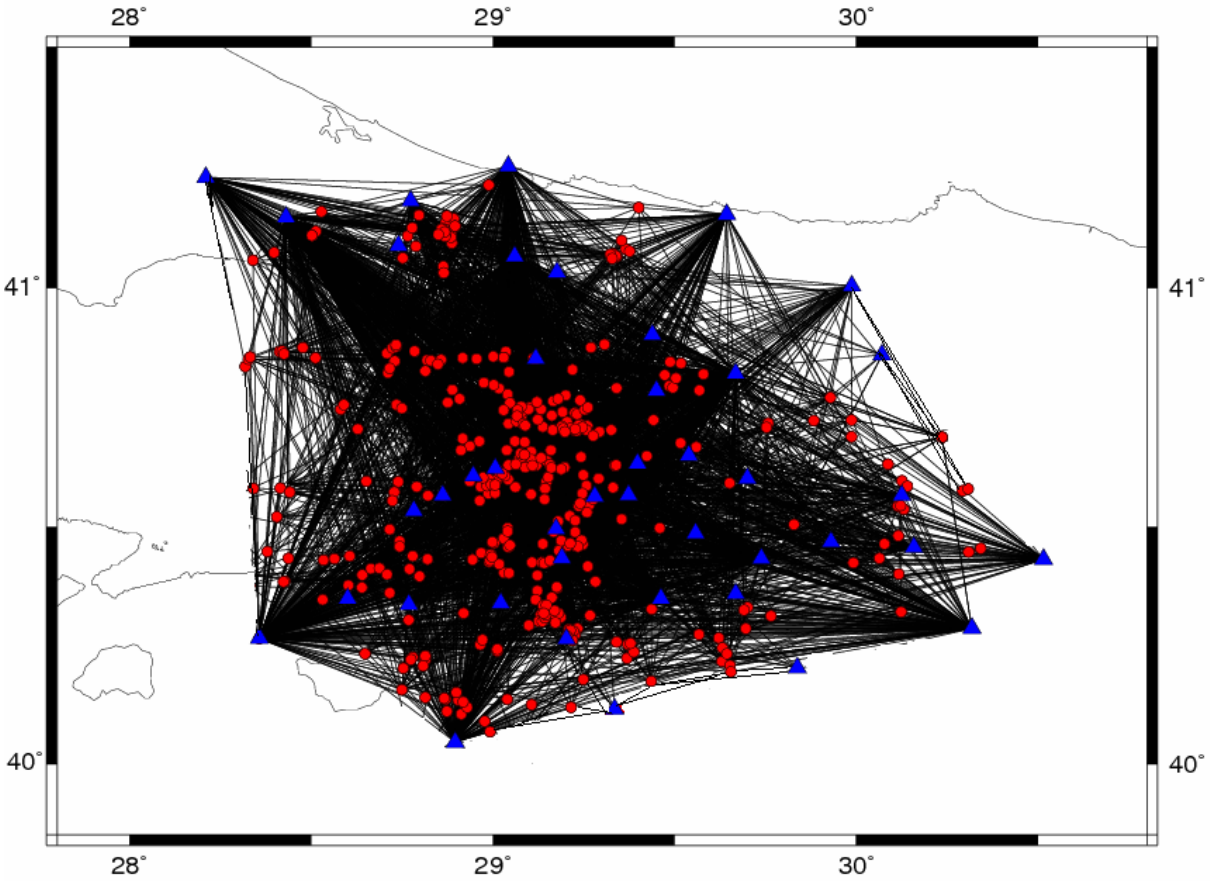

Figure 6.11. Ray coverage map in the area

Weighting values for travel time residuals were set as the checkerboard test for prefered cell sizes. Damping parameters were determined as 10 and 15 for 10×10 km and 15×15 km cell sizes, respectively. Iteration number was set as 5 for both models. After 5 iterations, the results of the 3-D tomograhic inversion were obtained. Average RMS of relocated events was 0.35 seconds and data variance according to initial model was 0.046 s^2 at the first iteration. Average RMS decraesed to 0.19 seconds, data variance reduced to 0.005 s^2 due to updated velocity model and earthquake location in 5th iterations for 15×15 km cell size. On the other hand, model variance increased from 0.032 to 0.05 $(km/s)^2$. For 10×10 block size, overdetermined matrix was solved after 5 iterations. RMS decreased from 0.25 to 0.19 seconds and data variance reduced from 0.042 to 0.012 s^2. At this time, model variance showed reduction from 0.046 to 0.034 $(km/s)^2$.

To understand the data quality, resolution parameters of real data set were analyzed. Ray hitcount, Derivative Weight Sum (DWS) and Resolution Diagonal Element (RDE) parameters were plotted for models. Figures 6.12 and 6.15 show calculated ray numbers in blocks for 10×10 km and 15×15 km models. Generally in every layer, areas in station network have a high ray coverage. The main purpose of plotting the hitcount map was to observe areas where a low number of rays passing. These parts of the study region are seen in Figures 6.12 and 6.15. Figures 6.13 and 6.16 show mapped DWS values which was calculated through inversion for the two models. Lower limit for DWS was determined as 1000. Depths below 17 km, DWS values were less than 1000 and blocks in these depths were not well resolved. Blocks which have a good resolving power correspond to 7.2, 12 and 17 km depths according to DWS criteria. High DWS values were observed in areas with a dense station coverage. DWS values increased with depths and reliable results were not observed depths below 17 km. To asess the resolution quality, RDE parameter changes in horizontal plane section were plotted at different depths. RDE values change between 0 and 1. Blocks which have RDE values close to 1 shows reliable resolving power. Calculated RDE values and its distribution for two models are shown in Figures 6.14 and 6.17. The highest values for RDE were observed at 7.2 and 12 km. At 17 km and depth below 17 km, RDE values decreased. Result of the assesment of resolution parameters show interpretable and reliable spaces which have RDE>0.2 and DWS>1000.

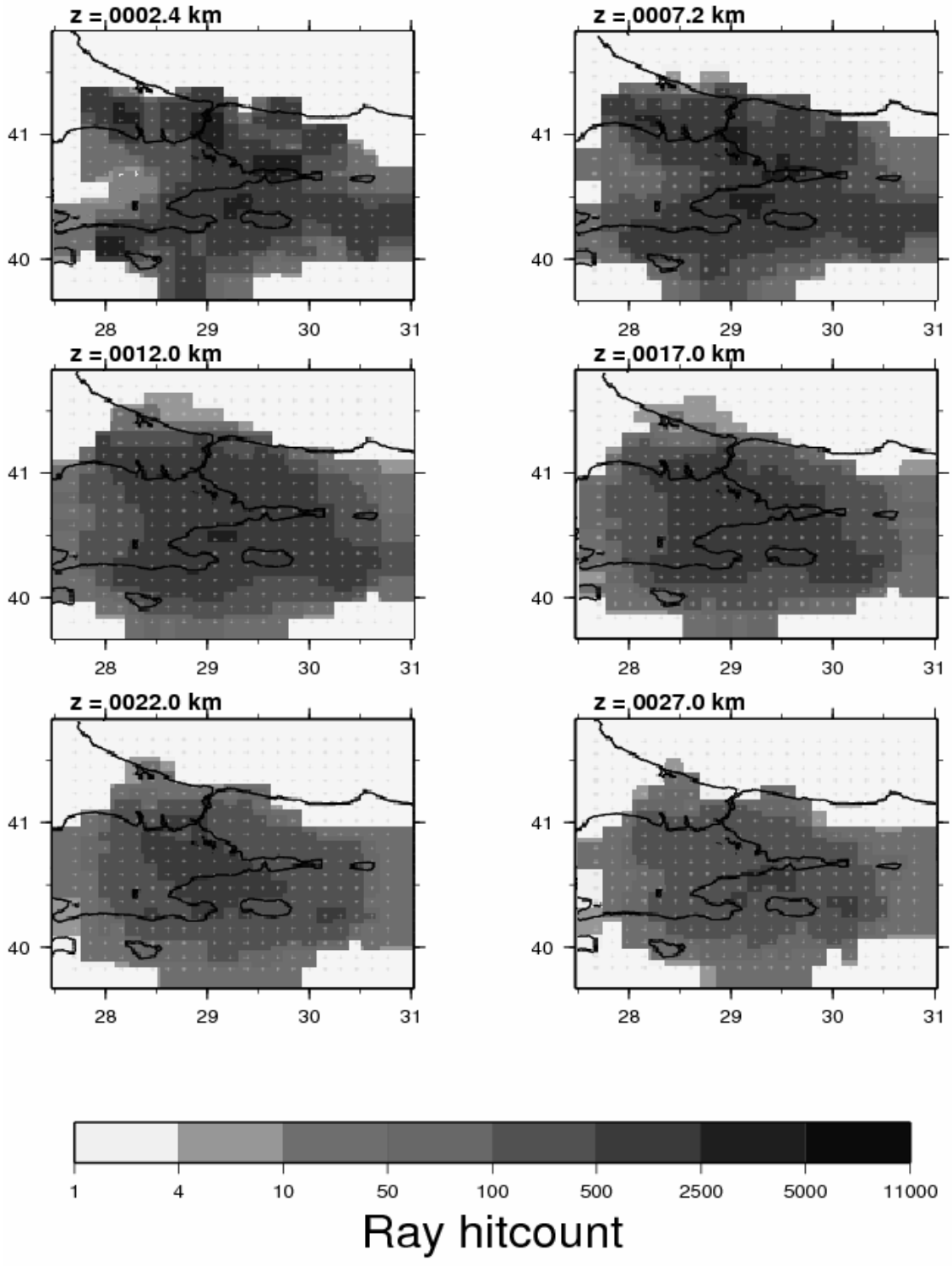

Figure 6.12. Hitcount map along horizontal plane sections for 10×10 km

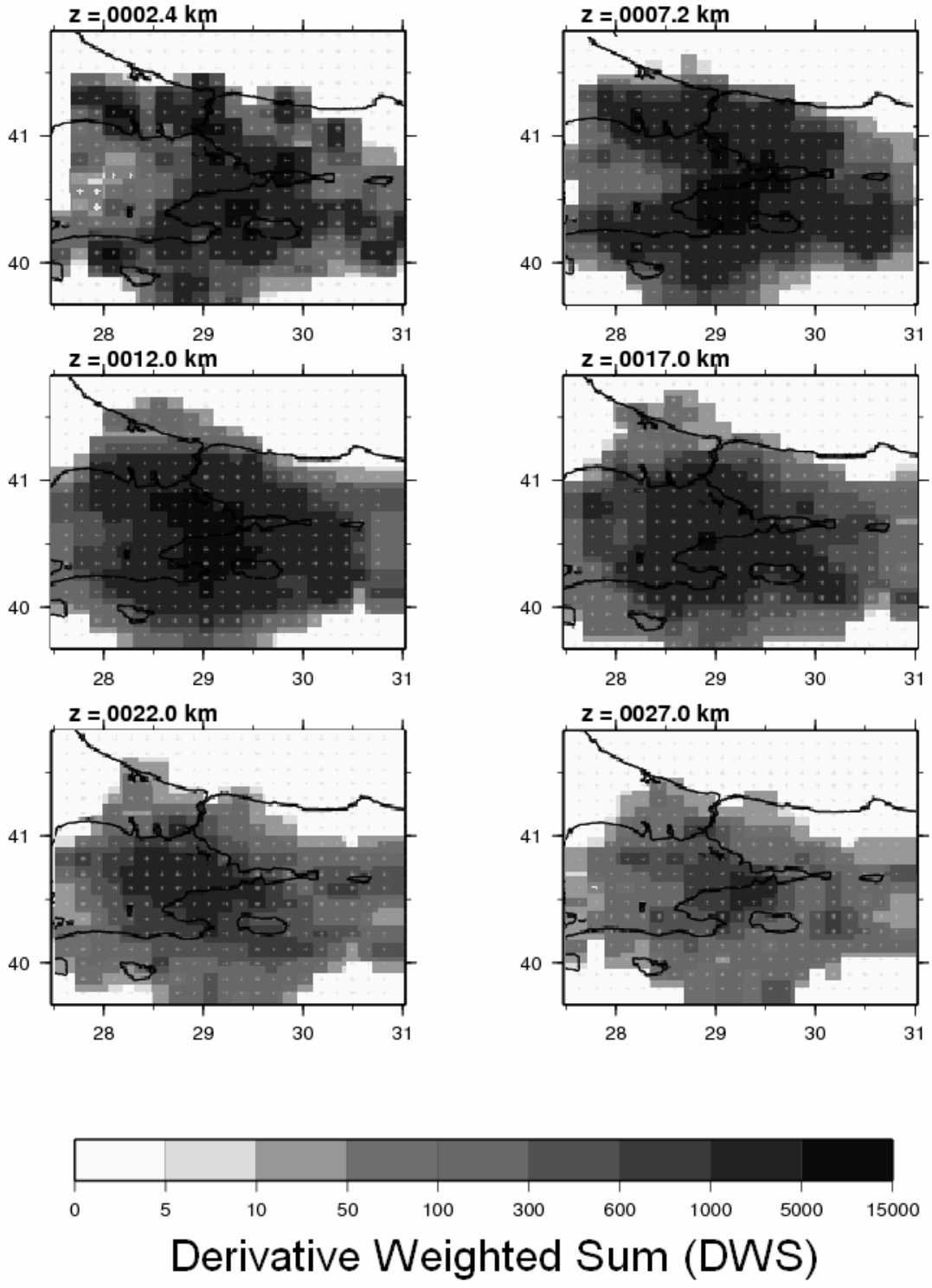

Figure 6.13. DWS changes along horizontal plane sections for 10×10 km

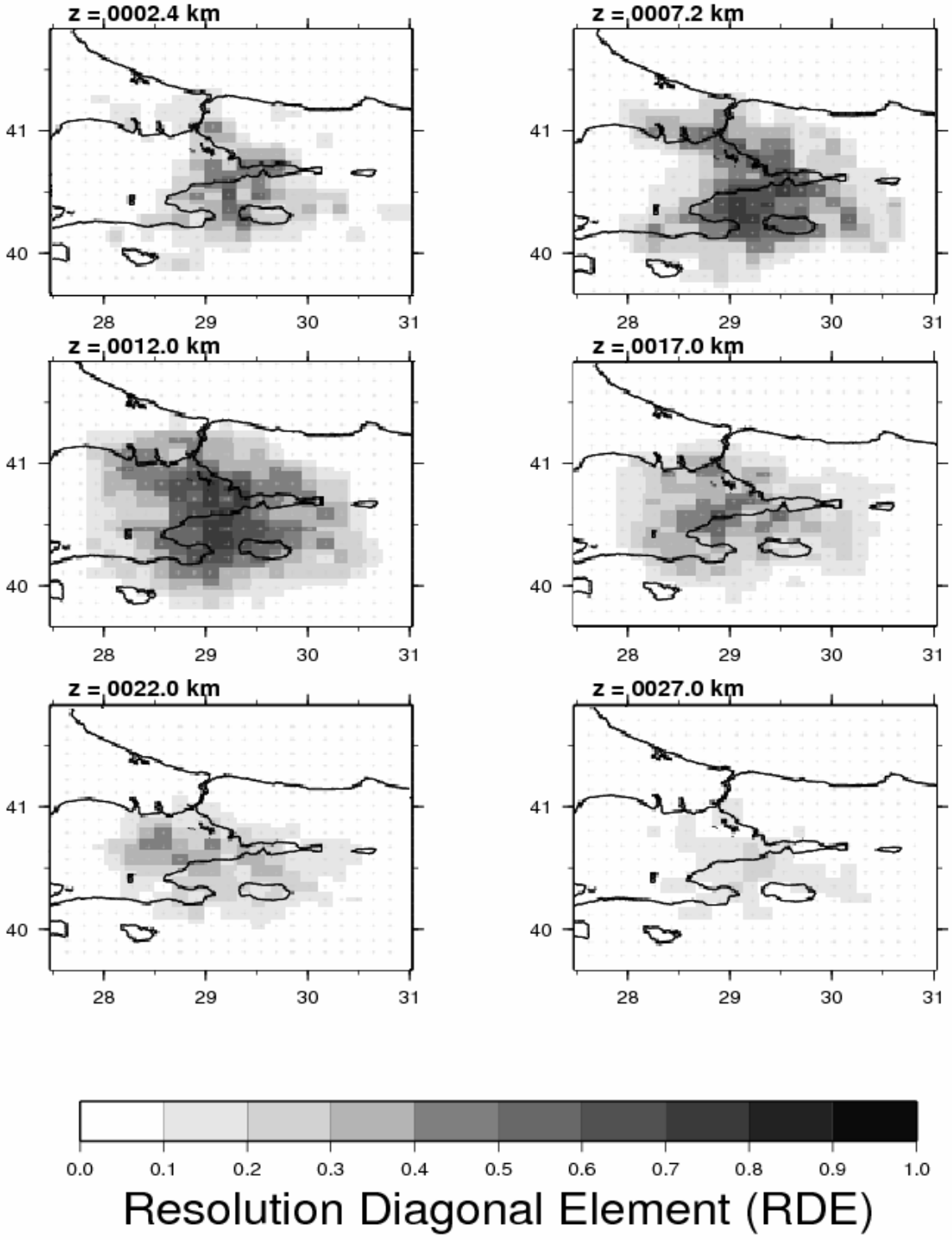

Figure 6.14. RDE changes along horizontal plane sections for 10×10 km

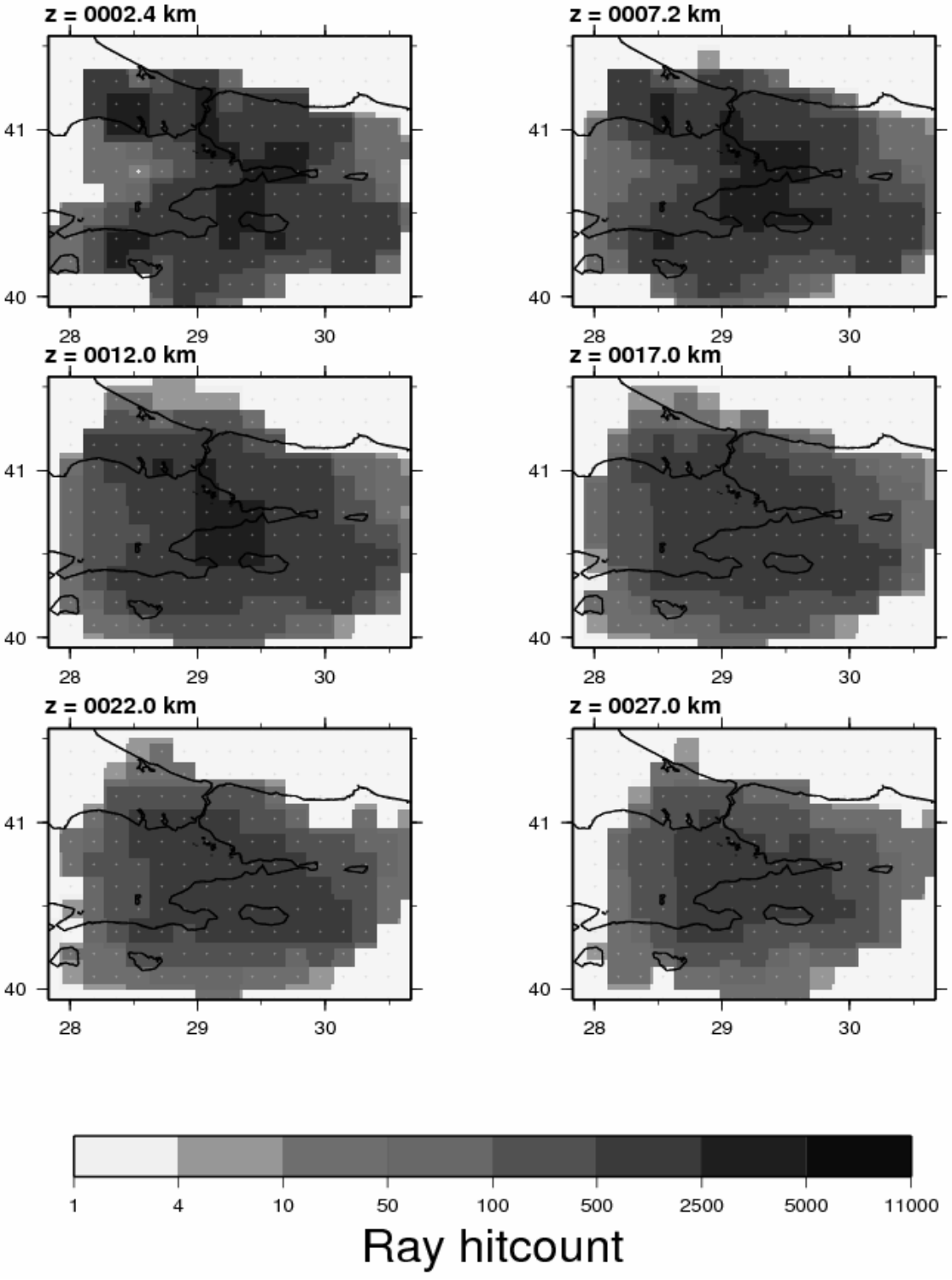

Figure 6.15. Hitcount map along horizontal plane sections for 15×15 km

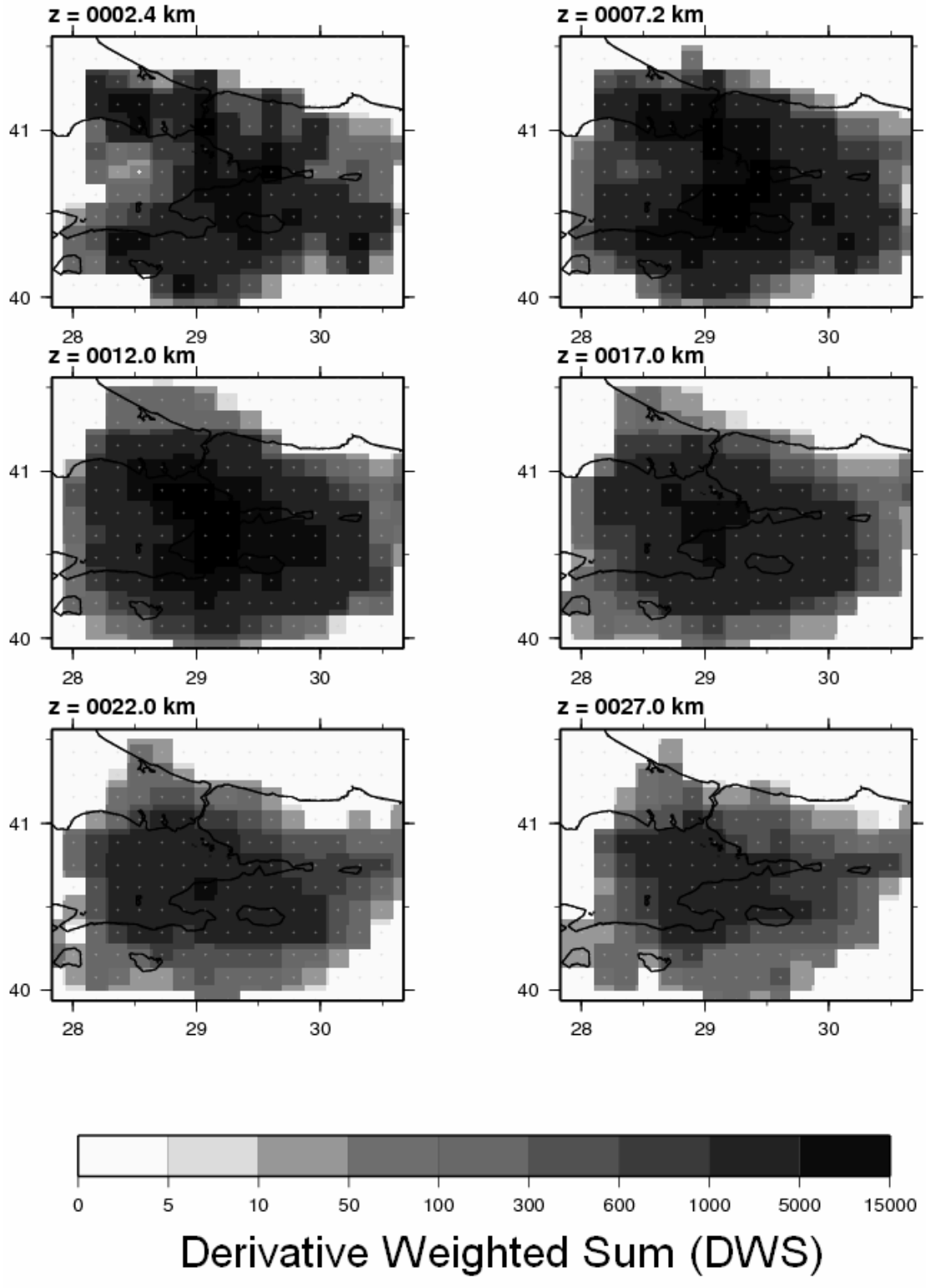

Figure 6.16. DWS changes along horizontal plane sections for 15×15 km

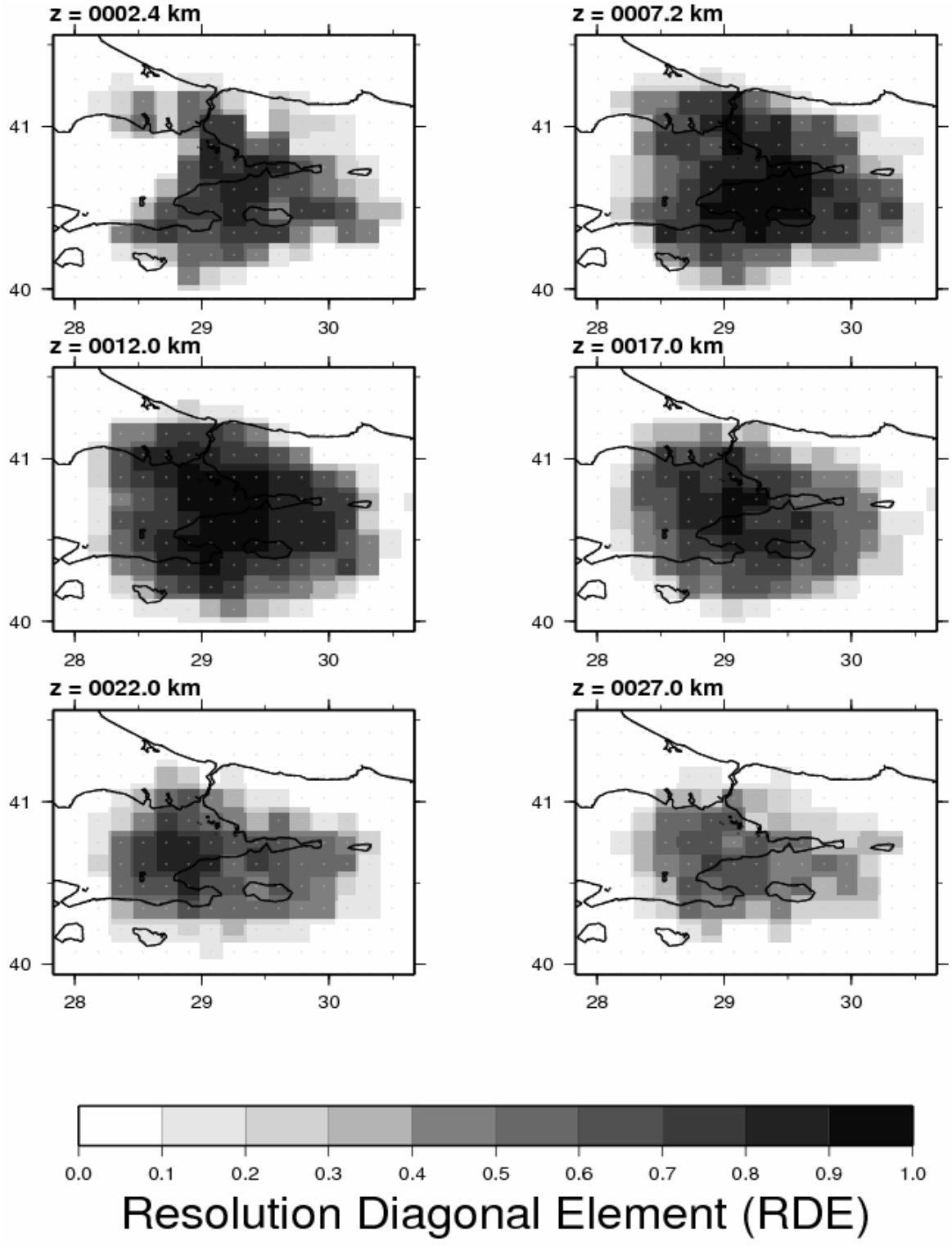

Figure 6.17. RDE changes along horizontal plane sections for 15×15 km

As a result of 3-D tomographic inversion, 3-D horizontal velocity changes were extracted for 10×10 km and 15×15 km as shown in Figures 6.18 and 6.19. Ray density coverage and crossing rays from different directions in cells are significant requirement to obtain a reliable and high resolution tomographic images. 22 and 27 km depths are not convenient to interpret velocity changes for these two models due to the lack of the data at these depths. On the other hand, depths to 17 km are interpretable when the results of the checkerboard test and resolution parameters of the data set are taken into account. Low and high velocity anomalies at these depths denote the similar locations for the two block sizes. Horizontal depth slices at 7.2 and 12 km has the high reliability and resolution compare with the other depth section due to intense earthquake locations.

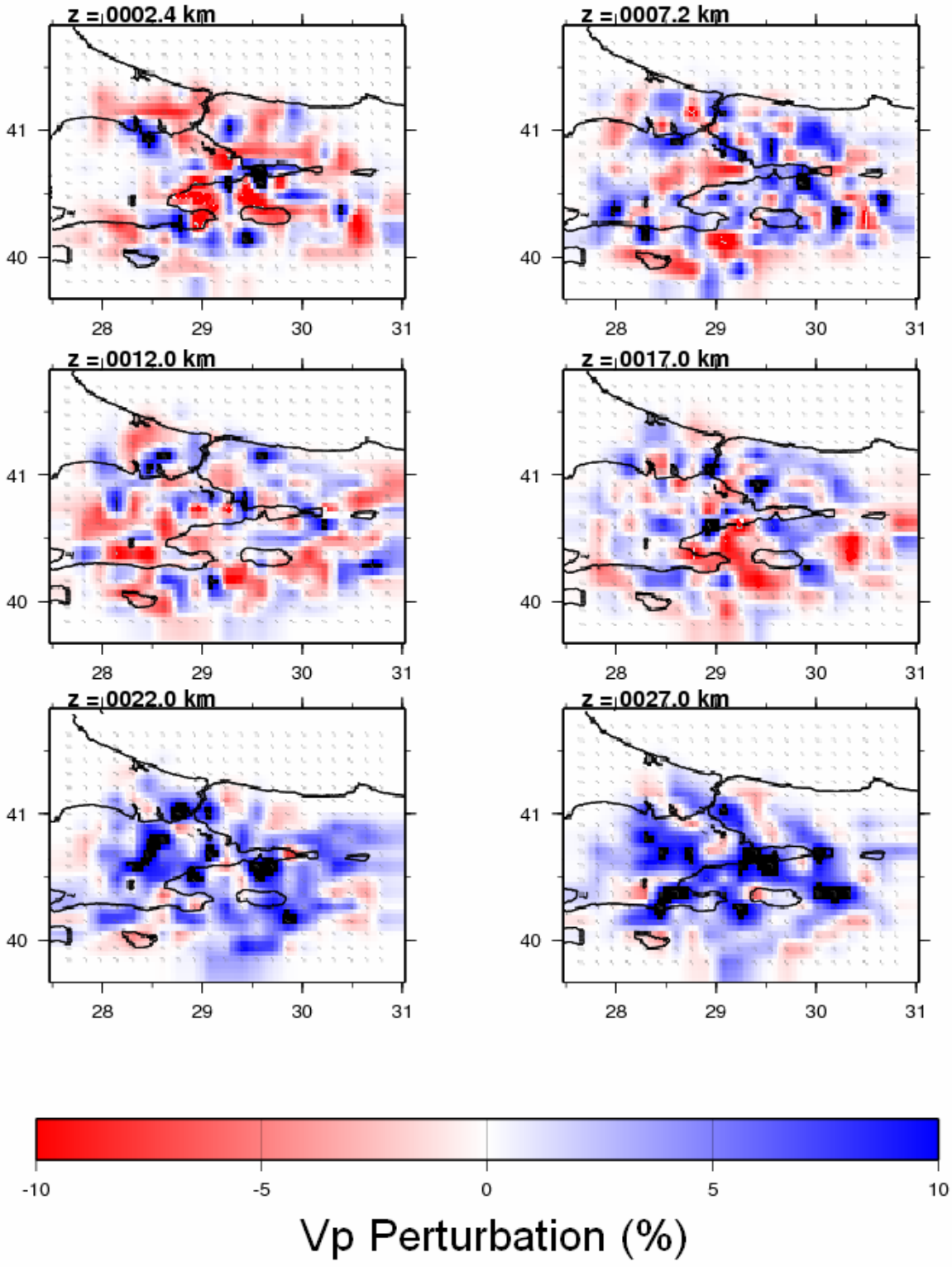

Figure 6.18. 3-D horizontal velocity changes for 10×10 km

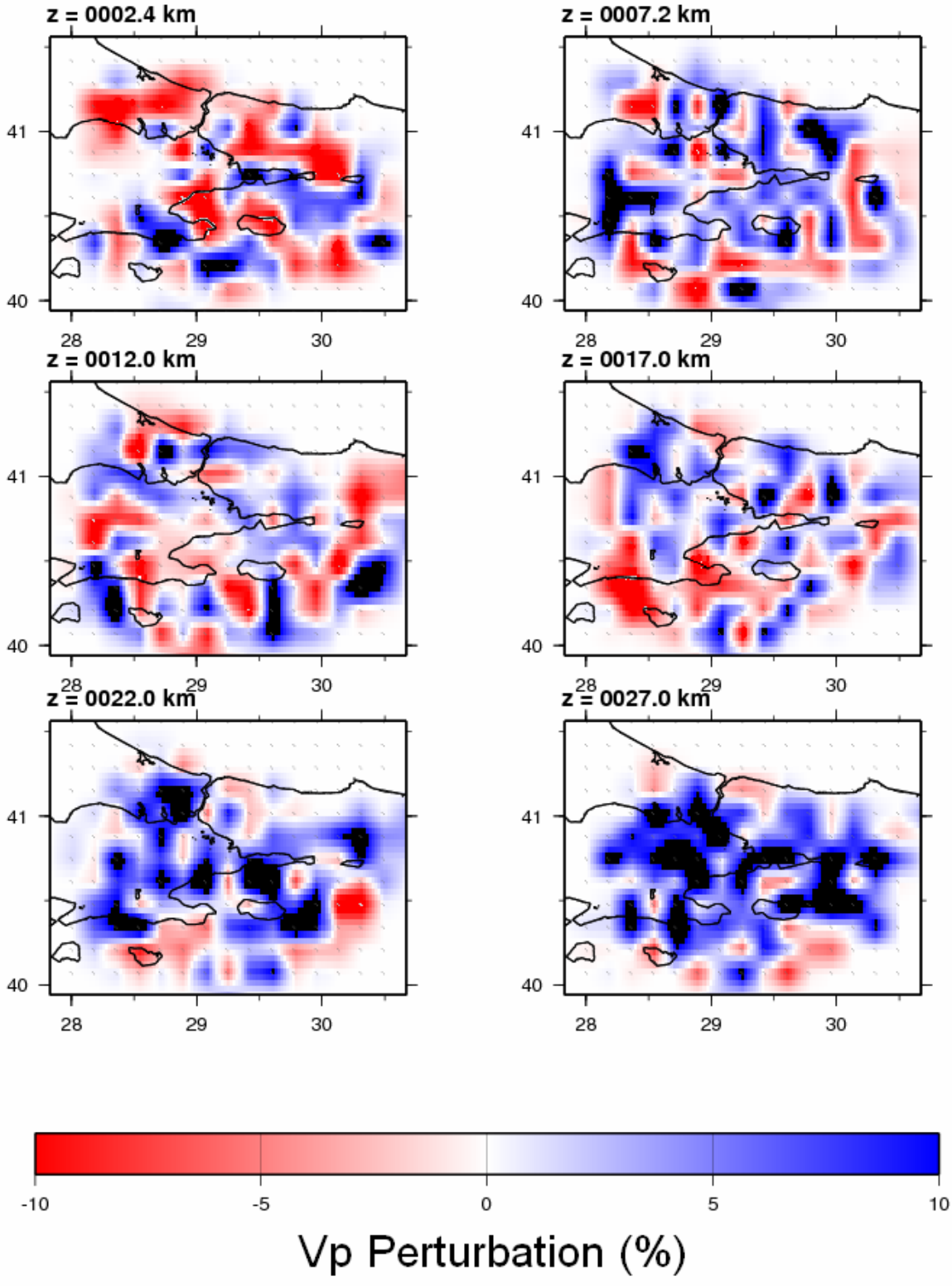

Figure 6.19. 3-D horizontal velocity changes for 15×15 km

Vertical depth sections along the profiles, N-S direction, were extracted to observe velocity structures. Profiles were generally constructed in a form of crossing the NAF branches (Figure 6.12). Tomographic images along the profiles were obtained for 10×10 km and 15×15 km cell sizes. Velocity structure along the cross sections were tried to interpret for 10×10 km model when the resolution compare with the 15×15 km cell size. All tomographic images along the profiles were contoured with white lines according to acceptable RDE value which was determined as 0.2. Interpretable portion of the figures were inner part of the RDE contours. All comment were realized under this criterian.

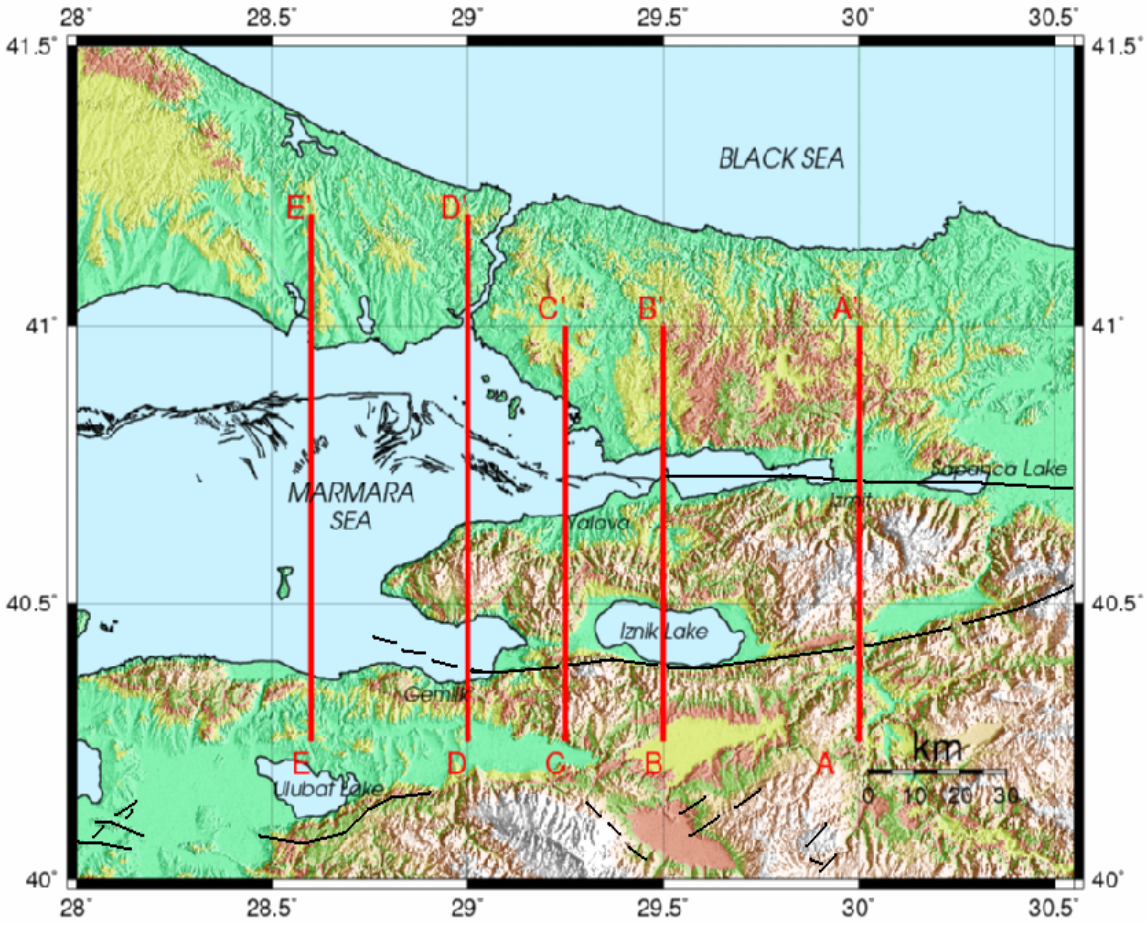

Figure 6.20. Faults in the region (Faults on the sea obtained LePichon *et al*., 2001. Faults on the land were modified by Esen Arpat)

Profiles AA' and BB' were constructed to observe south and north branches of the NAF. Tomographic images for the two profiles are shown in Figures 6.21 and Figure 6.22. In Figure 6.21, low velocity zone is observed between the depth range 2 and 15 km and it

is located approximately 55 km away from the south. It was approximately corresponds the fault zone located between İzmit and Sapanca. South branch of the NAF are not well observed as the northern branch. Only low velocities are seen at the localized zone between 0-20 km distances. This situation can be resulted from having nonuniform dense ray sampling along the profiles. In Figure 6.22, vertical extensions of the southern and northern branch of the NAF are observed as boundary between high and low velocity blocks. Location of these boundaries correspond projections of the two branches of the NAF on the surface relatively.

To observe the active parts of the NAF at the present day, profile CC' was constructed (Figure 6.23). Low velocity zones are located between 2 and 15 km. Low velocity zones between 0-20 km and 50-60 km distances show similarities with the location of southern and northern branch of the NAF, respectively. In this profile low velocity zones are surrounded with the high velocity blocks from south to north. Low and high velocity zones at the depth range between 2 km and 15 km generally correspond to high and low velocity zone, respectively under 15 km. This boundary along the 15 km is interpreted as the bottom of the seismogenic zone. Another profile, DD', was constructed. Vertical depth sections along the DD' show similarities with the profile CC' in terms of velocity structure locations of the low velocities which correspond to projection of localized branches of the NAF (Figure 6.24). Imaging the western part of the study region, profile EE' was constructed (Figure 6.25). Lowest velocities are observed from 20 to 70 km distance. Vertical extension of the low velocities between 2 and 15 km depths at the approximately 65 km distance is related to the northern branch of the NAF.

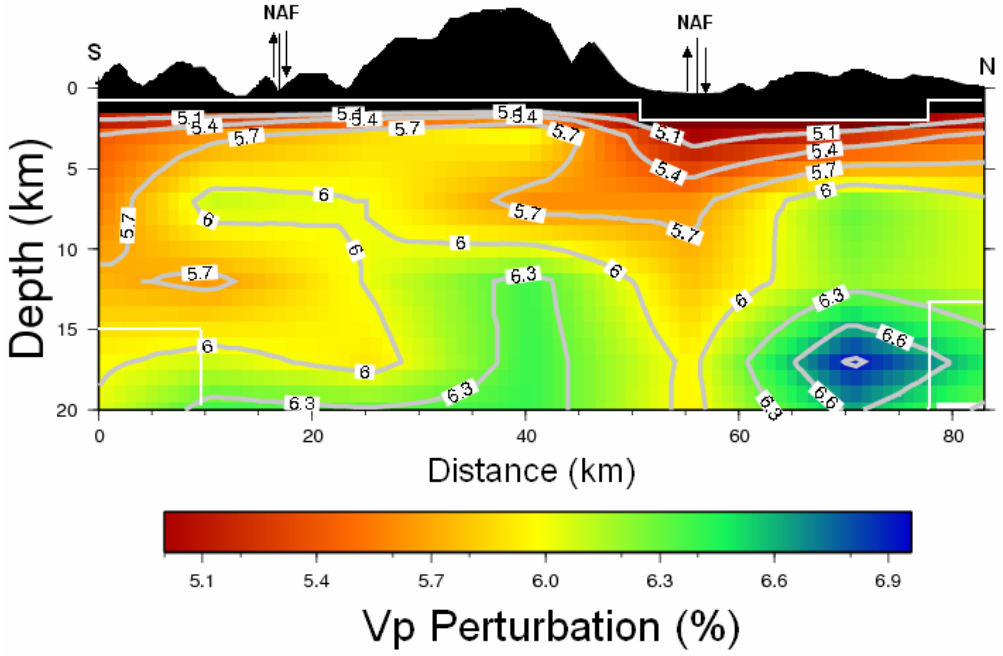

Figure 6.21. Vertical depth section along AA'

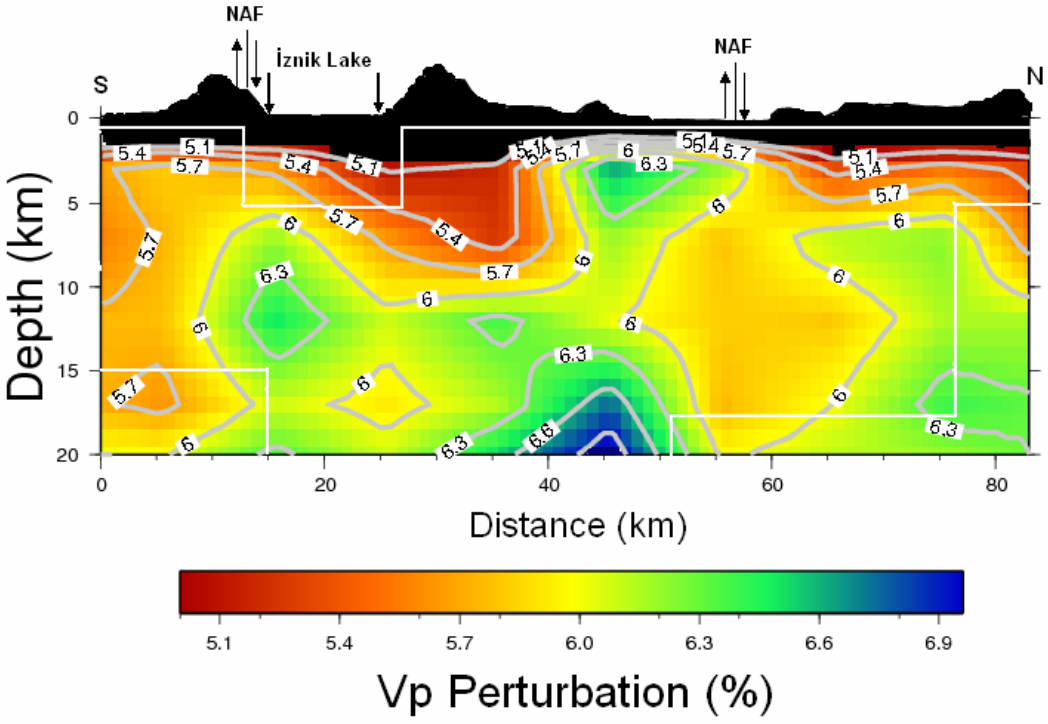

Figure 6.22. Vertical depth section along BB'

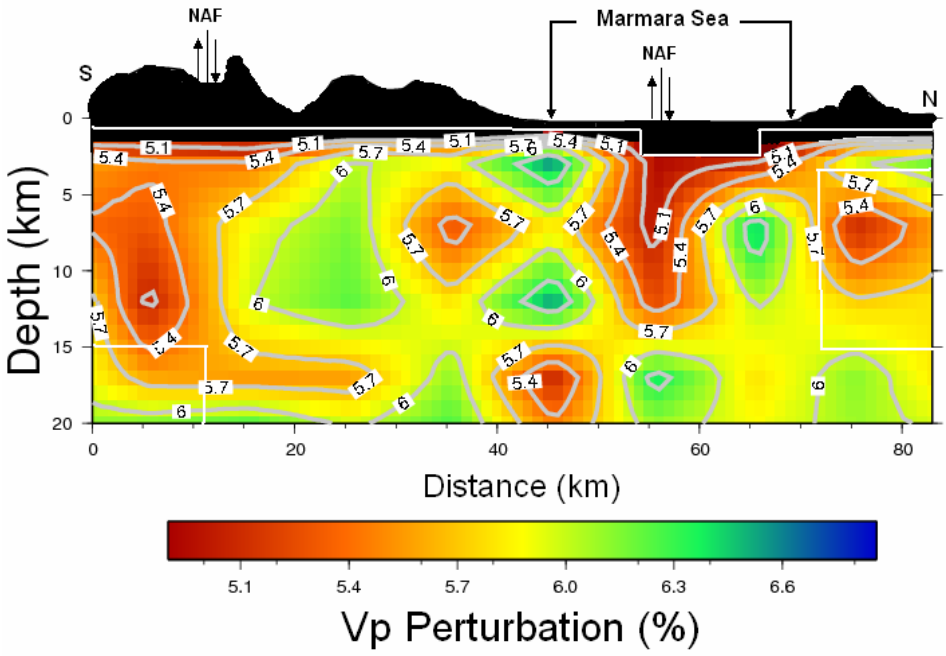

Figure 6.23. Vertical depth section along CC'

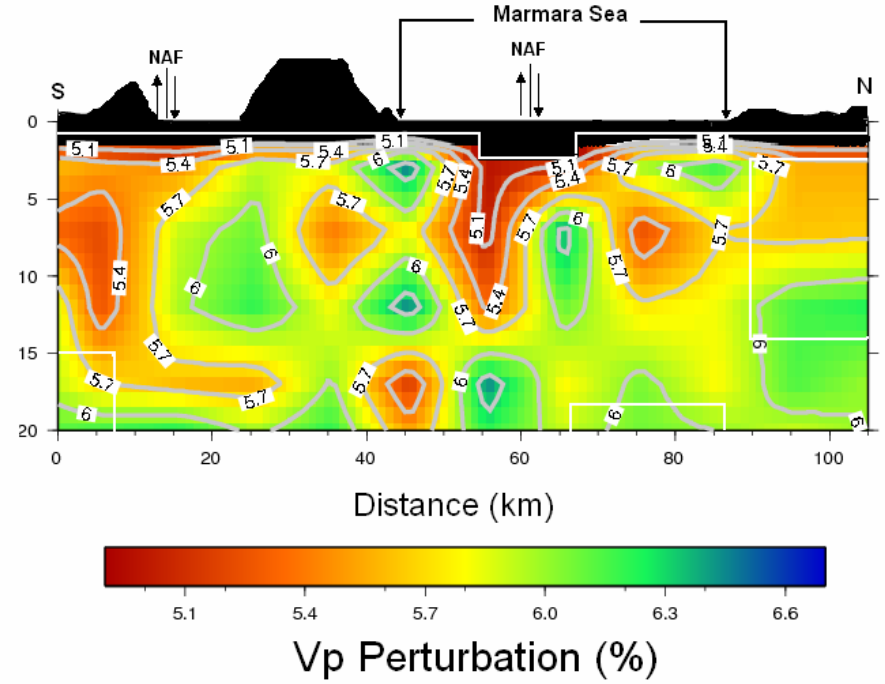

Figure 6.24. Vertical depth section along DD'

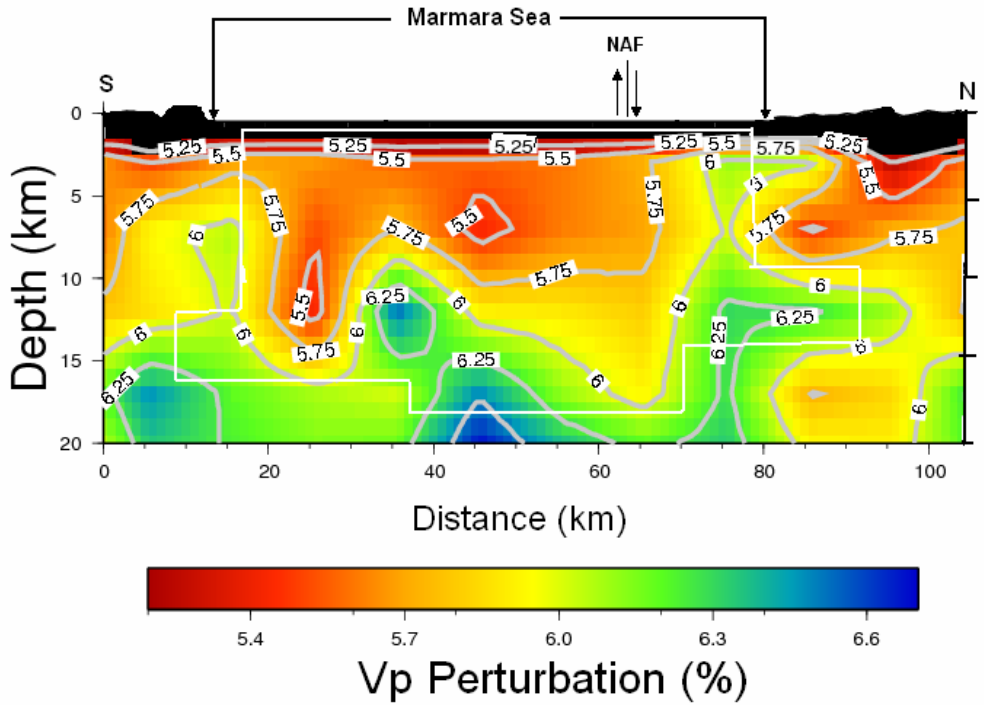

Figure 6.25. Vertical depth section along EE'

7. DISCUSSION AND CONCLUSION

The main purpose of this work is to reveal crustal velocity structure and information about the fault geometry in the study area. Earthquake data were collected from dispersely located seismic stations in the region between January, 2003 and October, 2007. 14329 P wave arrival times from 560 events were processed.

Collected data were used to obtain 1-D velocity model for local earthquake tomography. Crustal thickness is approximately 32 km for the study region. Reliable solutions were observed up to 17 km when the depth distributions of the earthquakes are taken into account. Checking the robustness of the velocity model, shifting test was applied to understand accurateness of the hypocenter locations and for the stability of the solution to the coupled problem. In addition to shifting test, quarry blast data were used to understand the robustness of the velocity model through checking the location precision. The results of these tests gave a reliable 1-D velocity model robustness for the study region. Obtained 1-D velocity model prefered as reference earth model for local earthquake tomography. Resolving power of data set with the reference earth model and synthetic data set were examined through the checkerboard tests to understand more confidential part of the velocity changes in the study region. Later on, tomographic images were interpreted according the resolution parameters of the real data set and the results of the checkerboard tests.

Low and high velocity zones were observed for interpretable horizontal depth sections at the similar locations. Vertical depth sections give information about the vertical extension of the velocity structure along the profiles. Obtaining this information, AA', BB', CC', DD' and EE' profiles were constructed in study area. Velocity structures beneath the profiles were tried to correlate with geologic structure in the region. Fault zones represented with low velocities at all vertical depth sections except profile BB'. In this profile, fault zone is observed as boundary between low and high velocity blocks. Tomographic images along profiles CC' and DD' have a consistency about locations of the low velocities which correspond to projection of localized branches of the NAF. Low velocities observed at the depth range between 2 and 15 km as localized zones. In these

profiles, a horizontal boundary plane is oberved at the depth of 15 km. Velocity zone corresponding the NAF is ended at the depth 15 km. This observation can be interpreted as the boundary of the seismogenic zone. Earthquakes which have high magnitudes generally occured the depth range between 15 and 17 km for this region in the past. This information is can be interpreted as the bottom of the seismogenic zone along the depth of 15 km.

To reveal the suspected fault zone between Marmara Sea and Black Sea, tomographic images along determined vertical cross sections were produced. Generally, produced images have a low resolution for the northern part of the section. Cross sections DD' and EE' have low velocity zones and they are located distances between 80 and 100 km. Low velocities are not observed in interpretable parts of the tomographic images along these profiles. Eventually, these low velocity zones are not possible to correlate with the suspected fault zone on the basis of our tomographic images.

In the study region, different geophysical applications were performed to reveal crustal model. Results obtained from tomographic images along vertical cross sections have a good correlation with the previous studies done in the region. The results obtained from the other geophysical studies are used to express the similarities and differences between the crustal models obtained from this study.

In section EE', low velocity zone is located approximately at 20 and 30 km distances and it takes place between 2 and 15 km depth range. This can be interpreted as former inactive fault zone. On the other hand, the northern side of the Armutlu peninsula bounded with the fault which is located on the MTA produced active fault map of Turkey. Observed former inactive fault zone along the cross section EE' can be accepted as continuation of this fault which was determined by MTA. In the Marmara region, Okay *et al*. (2000) studied the NAF system and the linked basins in the eastern Marmara Sea by using acquired multi-channel seismic reflection data. One of the results of this seismic experiment is correlated with our interpration about former inactive fault which is observed along the vertical cross section EE'. The fault which passes through the northern boundary of the Armutlu Peninsula can be accepted as the extention of the fault in the north of the Imrali Island.

Karabulut *et al*. (2003) revealed 2-D tomographic seismic velocity image in eastern Marmara region along 120 km long seismic refraction profile from Şile to Gemlik. Similar characteristic features are observed when compared with the crustal velocity structure along CC' . High velocities are located approximately underneath the Armutlu peninsula. The Armutlu peninsula is dominated by metamorphic assemblages (Yılmaz *et al*., 1995). High velocity block is observed below to 5 km beneath the Kocaeli Peninsula. This high velocities located below the İstanbul zone which is described by a well developed, unmetamorphosed and little deformed continuous Palezoic sedimantary succession extending from Ordovician to the Carboniferous age (Ketin, 1973 and Okay, 1986).

Another noteworthy study was performed by Nakamura *et al*. (2002). They used 1999 İzmit earthquake and aftershocks. Location of the profile AA' in this study match with the vertical cross section (AA') which traverses the southern and northern branches of NAF in our model. Low velocity zones are observed under the southern and northern branches of NAF at the similar depths between 2 and 15 km. One of the other geophysical application was performed by Tank *et al*. (2005). They collected the long period MT data along the profile which is the same location with the vertical cross section AA'. Results of the MT measurement along İzmit profile show that the low velocity zone at the depth to 5 km approximately correspond to resistive zone in crustal model produced by Tank *et al*. (2005). This shallow low resistive zone reflecting young sediments. Depths below 5 to 25 km, vertical extension of two branches correspond to boundary between high and low resistivity values. In our model, vertical extensions of the NAF branches correspond to low velocity zone. There is a difference between the crustal models for the same area. Relatively low resistivity values extends between the two branches of the NAF. This can be interpreted as high velocity zones indicating little fluid content and correspond to high resistivity zone in model produced by Tank *et al*. (2005).

REFERENCES

Aki, K., 1993. Overview. In: Iyer, H.M., Hirahara, K. (Eds.), Seismic Tomography: Theory and Practice. Chapman and Hall, London, pp. 1-6.

Aki, K., 1982. Three-dimensional inhomogeneities in the lithosphere and asthenosphere: evidence for decoupling in the lithosphere and flow in the asthenosphere., *Rev. Geophys. Space Phys.*, 20, 161-170.

Aki, K., Christofferson, A., and Husebye, E.S., 1976. Three-dimensional seismic structure of the lithosphere under Montana Lasa., *Bull. Seismol. Soc. Am.*, Vol. 66, pp. 501-524.

Aki, K., Lee, W.H.K., 1976. Determination of three-dimensional velocity anomalies under a seismic array using first P arrival times from local earthquakes 1. A homogeneous initial model., *Journal of Geophys. Res.*, Vol. 81, pp. 4381-4399.

Aktar, M., Dorbath, C., and Arpat, E., 2004. The seismic velocity and fault structure of the Erzincan basin, Turkey, using local earthquake tomography., *Geophys. J. Int.*, Vol. 156, pp. 497-505.

Ambraseys, N., 2002. The seismic activity of the Marmara Sea Region over the Last 2000 years., *Bull. Seismol. Soc. Am.*, Vol. 92, pp. 1-18.

Ambraseys, N., and Jackson, J.A., 2000. Seismicity of the Sea of Marmara (Turkey) since 1500., *Geophys. J. Int.*, Vol. 141, pp. F1-F6.

Ambraseys, N., Finkel, C.F., 1995. The Seismicity of Turkey Mediterranean. Middle East Abstracts, *IUGG, 21th Geneand Adjacent Areas*. Eren Yayincilik, Istanbul, Turkey.

Arpat, E., and Şentürk, E., 2003. İstanbul Yöresinin, Orta Eosen' den bu yana, Jeolojik Gelişiminin Ana Çizgileri (Geological Evolution of the İstanbul Region since Middle Eocene), *İstanbul' un Jeolojisi Sempozyumu Bildiriler Kitabı*, pp.39-48.

Barış, Ş., Nakajima, J., Hasegawa, A., Honkura, Y., Ito, A., and Üçer, B., 2005. Three-dimensional structure of Vp, Vs and Vp/Vs in the upper crust of the Marmara region, NW Turkey., *Earth Planets Space*, Vol. 57, pp. 1019-1038.

Barka, A.A., 1997. Neotectonics of the Marmara region in active tectonics of Northwest Anatolia. In: Schindler, C., Pfister, M. (Eds.), The Marmara Poly-project. *Hochschul-verlag AG an der ETH, Zurich*, pp. 55–87.

Barka, A., 1996. Slip distribution along the North Anatolian N., 1997. Seismicity and seismotectonics of the Bursa Area. fault associated with the large earthquakes of the period In: Schindler, C., Pfister, M. (Eds.), The Marmara Poly 1939 to 1967. *Bull. Seismol. Soc. Am.*, Vol. 86, pp. 1238–1254.

Barka, A., 1992. The North Anatolian Fault Zone., *Ann. Tectonicae*, Vol. 6, pp. 164-195.

Barka, A. and Kadinsky-Cade, K., 1988. Strike-slip fault geometry in Turkey and its influence on earthquake activity., *Tectonics*, Vol. 7, pp. 663-684.

Bekler, T. and Gürbüz, C., 2008. Insight into the Crustal Structure of the Eastern Marmara Region, NW Turkey., *Pure appl. Geophys.*, DOI 10.1007/s00024-008-0302-3

Buchanan, D.J., Davis, R., Jackson, P.J., and Taylor, P.M., 1981. Fault Location by Channel Wave Seismology in United Kingdom Coal Seams., *Geophysics*, Vol. 46, pp. 994-1002.

Canıtez, N., and Üçer, B. S., 1967. Computer determinations for the fault plane solutions in and near Anatolia., *Tectonophysics*, Vol. 4, pp. 235-244.

Cormack, A.M., 1973. Reconstruction of Densities from their Projections, with Applications in Radiological Physics., *Phys. Med. Biol*, Vol. 18, no. 2, pp. 195-207.

Crampin, S., and Evans, R., 1986. Neotectonics of the Marmara Sea region of Turkey, *J. Geol. Soc. Lond*. Vol. 243, pp. 343–348.

Crampin, S., and Üçer, B., 1975. The Seismicity of the Marmara Sea Region of Turkey., *Geophys. J. Roy. Astr. Soc.*, Vol. 40, pp. 269-288.

Deal, M. M. and Nolet, G., 1996. Comment on 'Estimation of resolution and covariance for large matrix inversions' by J. Zhang and G. A. McMechan., *Geophys. J. Int.*, Vol. 127, pp. 245-250.

Dewey, J.W., and Şengör, A.M.C., 1979. Aegean and surrounding regions; complex multiplate and continuum tectonics in a convergent zone., *Geol. Soc. Am. Bull.*, Part I, Vol. 90, pp. 84-92.

Dewey, J.W., 1976. Seismicity of Northern Anatolia., *Bull. Seismol. Soc. Am.*, Vol. 66, pp. 843-868.

Dines, K.A., and Lytle, J.R., 1979. Computerized geophysical tomography, *Proc. IEEE*, Vol. 67, no. 7, pp. 1065-1073.

Eberhart-Phillips, D., 1986. Three-dimensional velocity structure in Northern California coast ranges from inversion of local earthquake arrival times., *Bull. Seismol. Soc. Am.*, Vol. 76, pp. 1025-1052.

Evans, J.R., Eberhart-Phillips, D., and Thurber, C. H., 1993. User's Manual for SIMULPS12 for Imaging Vp and Vp/Vs: A Derivative of the "Thurber" Tomographic Inversion SIMUL3 for Local Earthquakes and Explosions., *U.S. Geological Survey Open File Report*, pp. 94-431.

Eyidoğan, H., 1988. Rates of crustal deformation in western Turkey as deduced from major earthquakes, *Tectonophysics*, Vol. 148**,** pp. 83–92.

Gürbüz, C., Aktar, M., Eyidoğan, H., Cisternas, A., Haessler, H., Barka, A., Ergin, M., Türkelli, N., Polat, O., Üçer, S.B., Kuleli, S., Barış, Ş., Kaypak, B., Bekler, T., Zor, E., Biçmen, F., Yörük, A., 2000. The seismotectonics of the Marmara region (Turkey): results from a microseismic experiment., *Tectonophysics*, Vol. 316, pp. 1-17.

Gürbüz, C., Püskülcü, S., and Üçer, B., 1991. A study of cruatal structure in the Marmara region using earthquake data, In: A.M. Işıkara and Y. Honkura [Editors], Multidisciplinary Research on Fault Activity in the Western Part of the North Anatolian Fault, *Boğaziçi University, Report-4*, pp. 29-41.

Gürbüz, C., 1985. Anadolu Kavağında Yapılan Taşocağı Patlatmalarından Elde Edilen Sismik Kayıtların Değerlendirilmesi, *Deprem Araştırma Bülteni*, Sayı 49, 39-49.

Gürbüz, C., Üçer, B., Özdemir, H., 1980. Adapazarı Yöresinde Yapılan Patlatma ile İlgili Ön Değerlendirme Sonuçları., *Deprem Araştırma Bülteni*, Sayı 31, 73-88.

Haslinger, F., Kissling, E., 2001. Investigating of 3-D ray tracing methods in local earthquake tomography., *Physics of the Earth and Planetary Int.*, Vol. 123, pp. 103-114.

Haslinger, F., 1999. Short Readme and Description of SIMULPS14., *Internal Report Institute of Geophysics*, ETH Zürich.

Haslinger, F., Kissling, E., Ansorge, J., Hatzfeld, D., Papadimitriou, E., Karalostas, V., Makropoulos, K., Kahle, H.-G., Peter, Y., 1999. 3D crustal structure from local earthquake tomography around the Gulf of Arta (Ionian region, NW Greece)., *Tectonophysics*, Vol. 304, pp. 201-218.

Hole, J.A., 1992. Nonlinear High-Resolution Three-Dimensional Seismic Travel Time Tomography., *Journal of Geophys. Res.*, Vol. 97, pp. 6553-6562.

Honkura,Y., Isikara, A.M., Oshiman, N., Ito, A., Ucer, B., Baris, S., Tuncer, M.K., Matsushima, M., Pektas, R., Celik, C., Tank, S.B., Takahashi, S., Nakanishi, F., Yoshimura, R., Ikeda, Y., Komut, T., 2000. Preliminary results of multidisciplinary observations before, during and after the Kocaeli (İzmit) earthquake in the western part of North Anatolian Fault Zone., *Earth Planets Space*, Vol. 52, pp. 293-298.

Hoşgören, M.Y., 1997. Geomorphology of basin of the Gulf of İzmit. *İzmit Körfez'inin Kuvaterner stifi, Gölcük.*, pp. 343-348.

Hounsfield, G.N., 1973. Computerized transverse axial scanning (tomography). 1. description of system., *Br. J. Radiol.*, Vol.46, no. 552, pp. 1016-1022.

Humpreys, E., and Clayton, R.W., 1988. Adaption of Back Projection Tomography to Seismic Travel Time Problems., *Journal of Geophys. Res.*, Vol. 93, pp. 1073-1085.

Husen, S., 1999. Local Eartquake Tomography of a Convergent Margin, North Chile: A Combined On-and Offshore Study, Ph. D. Thesis, Christian-Albrechts University, Kiel.

Husen, S., Kissling, E., 2001. Local earthquake tomography between rays and waves: fat ray tomography., *Physics of the earth and Planetary Int.*, Vol. 123, pp. 129-149.

Husen, S., Kissling, E., Flueh, E., and Asch, G., 1999. Accurate hypocentre determination in the seismogenic zone of the subducting Nazca Plate in northern Chile using a combined on-/offshore network., *Geophys. J. Int.*, Vol. 138, pp. 687-701.

Husen, S., Quintero, R., Kissling, E., and Hacker, B., 2003. Subduction zone structure and magmatic processes beneath Costa Rica constrained by local earthquake tomography and petrological modelling., *Geophys. J. Int.*, Vol. 155, pp. 11-32.

Karabulut, H., Bouin, M-P., Bouchon, M., Dietrich, M., Cornou, C., and Aktar, M., 2002. The seismicity in the Eastern Marmara Sea after the 17 August 1999 İzmit Earthquake., *Bull. Seismol. Soc. Am.*, Vol. 92, pp. 387-393.

Karabulut, H., Özalaybey, S., Taymaz, T., Aktar, M., Selvi, O., Kocaoğlu, A., 2003. A tomographic image of the shallow crustal structure in the Eastern Marmara., *Geophys. Res. Lett.*, Vol. 30, pp. 10-1–10-4.

Ketin, İ., 1973. Genel Jeoloji (General Geology), *Published by İTÜ, 4th Ed*.

Kissling, E., Husen, S., and Haslinger, F., 2001. Model parametrization in seismic tomography: a choice of consequence fort he solution quality., *Physics of the Earth and Planetary Int.*, Vol. 123, pp. 89-101.

Kissling, E., 1995. Velest User's Guide. Internal report, *Institute of Geophysics, ETH Zurich*, pp. 26.

Kissling, E., Ellsworth, W.L., Eberhart-Phillips, D., and Kradolfer, U., 1994., Initial reference models in local earthquake tomography., *Journal of Geophys. Res*., Vol. 99, pp. 19.635-19.646.

Kormendi, A., Bodoky, T., Hermann, L., Dianisda, L., and Kalman, Y., 1986. Seismic Measurements for Safety in Mines, Geophysical Prospecting, Vol. 34, pp. 1022-1037. Laigle, M., Hirn, A., Sapin, Lepine, J.C., Diaz, J., Gallart, J., and Nicolich, R., 2000. Mount Etna dense array local earthquake P and S tomography and implications for volcanic plumbing., *Journal of Geophys. Res.*, Vol. 105, pp. 21.633-21.645.

Le Pichon, X., Şengör, A.M.C., Demirbağ, E., Rangin, C., İmren, C., Armijo, R., Görür, N., Çağatay, N., Mercier de Lepinay, B., Meyer, B., Saatçılar, R., Tok, B., 2001. The active Main Marmara Fault., *Physics of the Earth and Planetary Int.*, Vol. 192, pp. 595-616.

Lee, W. H. K., and Lahr, J. C., 1975. HYP071 (Revised): a computer program for determining hypocenter, magnitude, and first motion pattern of local earthquakes, *U. S. Geological Survey Open File Report*, pp. 75-311.

Leveque, J.J., Rivera, L., and Wittlinger, G., 1993. On the use of the checkerboard test to assess the resolution of tomographic inversions., *Geophys. J. Int.*, Vol. 115, pp. 313-318.

Levin, K.F. And Lines, R.L.. Inversion of Geophysical Data, *Geophysics reprint series No.9*

Mason, I.M., 1981. Algebraic Reconstruction of a Two-Dimensional Velocity Inhomogeneity in the High Hazles Seam at Thoresby Colliery, *Geophysics*, Vol. 46, pp. 298-308.

McKenzie, D.P., 1972. Active tectonics of Mediterranean region., *Geophys. J. R. Ast. Soc.*, Vol. 30, pp. 109-185.

McClusky, S., Balassanian, S., Barka, A., Demir, C., Ergintav, S., Georgiev, I., Gürkan, O., Hamburger, M., Hurst, K., Kahle, H., Kastens, K., Kekelidze, G., King, R., Kotzev, V., Lenk, O., Mahmoud, S., Mishin, A., Nadariya, M., Ouzounis, A., Paradissis, D., Peter, Y., Prilepin, M., Reilinger, R., Şanlı, I., Seeger, H., Taeleb, A, Toksöz, M.N., and Veis, G., 2000. Global Positioning system constraints on plate kinematics and dynamics in the eastern Mediterranean and Caucasus., *J. Geophys. Res.*, Vol. 105, pp. 5695-5719.

Nakamura, A., Hasegewa, A., Ito, A., Üçer, B., Barış, Ş., Honkura, Y., Kono, T., Hori, S., Pektaş, R., Komut., T., Çelik, C., and Işıkara A.M., 2002. P-wave velocity structure of the crust and Its relationship to the occurance of the 1999 Izmit, Turkey, Earthquake and Aftershocks., *Bull. Seismol. Soc. Am.*, Vol. 92, pp. 330-338.

Okay, A.I., Kaşlılar-Özcan, A., İmren, C., Boztepe-Güney, A., Demirbağ, E, and Kuscu, I., 2000. Active faults and evolving strike-slip basins in the Marmara Sea, northwest Turkey: a multichannel seismic reflection study, *Tectonophysics*, Vol. 321, pp. 189-218.

Okay, A. I., Demirbağ, E., Kurt, H., Okay, N., and Kuşçu, I., 1999. An active, deep marine strike-slip basin along the North Anatolian Fault, Turkey., *Tectonics*, Vol. 18, pp. 129–147.

Okay, A.I., 1986. Tectonics Units and sutures in the pontides, Northern Turkey.Tectonic evolution of the Tethyan Region, *Nato ASI Series.*, Series C-Vol.259, pp. 109-116.

Özalaybey, S., Ergin, M., Aktar, M.,Tapırdamaz, C., Biçmen, F., and Yörük, A., 2002. The 1999 İzmit Earthquake Sequence in Turkey: Seismological and Tectonic Aspects., *Bull. Seismol. Soc. Am.*, Vol. 92, pp. 376-386.

Oztin, F., and Bayulke, N., 1990. Historical earthquakes of İstanbul and corrections to the original version. Kayseri and Elazig. *In: Turkish Atomic Energy Authority (Ed.)*, Proceedings of Workshop on Historical Seismicity and Seismotectonics of the Mediterranean Region 10–12 October 1990, Istanbul.

Paige, C.C., Saunders, M.A., 1982. LSQR: An algorithm for Sparse Linear Equations and Sparse Least Squares., *ACM Transactions on Mathematical Software*, Vol. 8, pp. 43-71.

Radon, J., 1917. Uber die bestimmung von functionen durch ihre integralwere lange gewisser mannigfaltigkeiten., *Ber. Verh. Saechs. Akad. Wiss.*, Vol. 69, pp. 262-267.

Raffaele, R., Langer, H., Gresta, S., and Moia, F., 2006. Tomogprahic inversion of local earthquake data from the Gioia Tauro basin (south-western Calabria, Italy)., *Geophys. J. Int.*, Vol. 165, pp. 167-179.

Smith, A. D., Taymaz, T., Oktay, F., Yüce, H., Alpar, B., Basaran, H., Jackson, A. J., Kara, S, and Şimşek, U., 1995. High resolution seismic profiling in the Sea of Marmara (NW Turkey): Late Quaternary sedimantation and sea level changes, *GSA Bull.*, Vol. 107/8., pp. 923-936.

Spakman, W., Bijwaard, H., 2001. Optimization of Cell Parametrization for Tomographic Inverse Problems., *Pure appl. Geophys.*, Vol. 158, pp. 1401-1423.

Straub, C., and Kahle, H.G., 1996. Global Positioning System (GPS) estimates of crustal deformation in the Marmara Sea Region, Northwestern Anatolia., *Earth Planet. Sci. Lett.*, Vol. 121, pp. 495-502.

Şengör, A.M.C., Görür, N., and Şaroğlu, F., 1985. Strike slip faulting and related basin formation in zones of tectonic escape: Turkey as a case study., *Soc. Econ. Paleont. Min. Spec. Pub.*, Vol. 37, pp. 227-264.

Tank, S.B., Honkura, Y., Ogawa, Y., Matsushima, M., Oshiman, N., Tunçer, M.K., Çelik, C., Tolak, E., Işıkara, A.M., 2005. Magnetotelluric imaging of the fault rupture area of the 1999 Izmit (Turkey) earthquake., *Physics of the Earth and Planetary Int.*, Vol. 150, pp. 213-225.

Taymaz, T., Jackson, J., and McKenzie, D., 1991. Active tectonics of the north and central Aegean Sea, *Geophys. J. Int.*, Vol. 106, pp. 433–490.

Thurber, C.H., 1983., Earthquake Locations and Three-Dimensional Crustal Structure in the Coyote Lake Area, Central California., *Journal of Geophys. Res.*, Vol. 88, pp. 8226-8236.

Thurber, C.H., 1992., Hypocenter-velocity structure coupling in local earthquake tomography., *Physics of the Earth and Planetary Int.*, Vol. 75, pp. 55-62.

Thurber, C.H., 1993. Local earthquake Tomography: velocities and Vp/Vs theory. In: Iyer, H.M., Hirahara, K. (Eds.), Seismic Tomography: Theory and Practice. Chapman and Hall, London, pp. 563-583.

Ucer, B., Eyidogan, H., Gurbuz, C., Barka, A., Serif, B., 1997. Seismic investigations of Marmara region in Active Tectonics of northwest Anatolia., In: Schindler, C., Pfister, M. (Eds.), The Marmara Poly-project. *Hochschulverlag AG an der ETH*, Zurich, pp. 55-87.

Virieux, J., 1991. Fast and accurate ray tracing by Hamiltonian Perturbation., *Journal of Geophys. Res.*, Vol. 96, pp. 579-594.

Westman, E.C. and Haramy, K.Y., 1996. Seismic tomography to map hazards ahead of the longwall face, *Mining Engineering*, Vol. 48, No. 11, pp. 73-79.

Westman, E.C., Haramy, K.Y., and Rock, A.D., 1996. Seismic tomography for longwall stress analysis, *Proceedings of 2nd North American Rock Mechanics Symposium 4 (Montreal, Quebec, June 19-21)*, ed. By M. Aubertin, F. Hassani, and H. Mitri, A.A. Balkema, pp. 397-403.

Wong, H. K., Lüdmann, T., Uluğ, A., and Görür, N., 1995. The Sea of Marmara: a plate boundary sea in an escape tectonic regime., *Tectonophysics*, Vol. 244, pp. 231–250.

Yao, Z.S., Roberts, R.G., and Tryggvason, A., 1999. Calculating resolution and covariance matrices for seismic tomography with the LSQR method., *Geophys. J. Int.*, Vol. 138, pp. 886-894.

Yılmaz, Y., Genç, S.C., Yiğitbaş, E., Bozcu, M., and Yilmaz, K., 1995. Geological evolution of the late Mesozoic continental margin of Northwestern Anatolia, *Tectonophysics*, Vol. 243, pp. 155-171.

Zhao, D., and Kayal, J.R., 2000. Impact of seismic tomography on earth sciences., *Current Science*, Vol. 79, pp. 1208-1214.

Zor, E., Özalaybey, S., and Gürbüz, C., 2006. The crustal structure of the eastern Marmara region, Turkey by teleseismic receiver functions., *Geophys. J. Int.*, Vol. 167, pp. 213-222.